

SeisMIC - an Open Source Python Toolset to Compute Velocity Changes from Ambient Seismic Noise

Peter Makus  * ^{1,2}, Christoph Sens-Schönfelder  ¹

¹Helmholtz Center, German Research Center for Geosciences GFZ, Potsdam, Germany, ²Institute for Geological Sciences, Freie Universität Berlin, Berlin, Germany

Author contributions: *Conceptualization*: PM, CS. *Methodology*: CS, PM. *Software*: PM, CS. *Formal Analysis*: PM. *Writing - Original draft*: PM. *Writing - Review & Editing*: CS. *Supervision*: CS. *Funding acquisition*: CS.

Abstract We present SeisMIC, a fast, versatile, and adaptable open-source software to estimate seismic velocity changes from ambient seismic noise. SeisMIC includes a broad set of tools and functions to facilitate end-to-end processing of ambient noise data, from data retrieval and raw data analysis via spectrogram computation, over waveform coherence analysis, to post-processing of the final velocity change estimates. A particular highlight of the software is its ability to invert velocity change time series onto a spatial grid, making it possible to create maps of velocity changes. With the software, we implement new data formats ensuring uniformity, flexibility, interoperability, and integrity. To tackle the challenge of processing large continuous datasets, SeisMIC can exploit multithreading at high efficiency with an about five-time improvement in compute time compared to MSNoise, probably the most widespread ambient noise software. In this manuscript, we provide a short tutorial and tips for users on how to employ SeisMIC most effectively. Extensive and up-to-date documentation is available online. Its broad functionality combined with easy adaptability and high efficiency make SeisMIC a well-suited tool for studies across all scales.

1 Introduction

Over the past twenty years, the analysis of temporal changes in seismic velocity has become a standard tool in seismology. Seismologists exploit records of repeating sources, such as explosives (e.g., Nishimura et al., 2000; Hirose et al., 2017), vibrators (e.g., Clymer and McEvelly, 1981; Ikuta et al., 2002), airguns (e.g., Wegler et al., 2006; Yang et al., 2018), or earthquake doublets (e.g., Poupinet et al., 1984; Sawazaki et al., 2015), to quantify such changes. Commonly, the analysis of delays focuses on the later arriving, multiply scattered wave train - the so-called coda, which samples the medium to a greater spatial extent than the first-arriving energy and is sensitive even to minute velocity changes (dv/v) in the order of per-mills (Snieder et al., 2002). We refer to this technique as coda wave interferometry.

*Corresponding author: makus@gfz-potsdam.de

31 While active source coda wave interferometry accurately resolves dv/v , studies using artificial sources are logis-
32 tically challenging and expensive. Repeating natural sources, on the other hand, rarely occur in regular patterns,
33 allowing only for a coarse temporal resolution of dv/v in seismically active regions. [Sens-Schönfelder and Wegler](#)
34 (2006) obtained dv/v by analysing modifications in the correlations of continuous waveforms. Their method, pas-
35 sive image interferometry (PII), relies on the diffusive energy field of the ubiquitous ambient seismic noise ([Sens-](#)
36 [Schönfelder and Wegler, 2011](#)). PII has successfully been applied to quantify velocity changes, for example due to
37 seasonal meteorological cycles (e.g., [Sens-Schönfelder and Wegler, 2006](#); [Wang et al., 2017](#)), earthquake damage (e.g.,
38 [Brennguier et al., 2008](#); [Minato et al., 2012](#)), volcanic deformation (e.g., [Sens-Schönfelder et al., 2014b](#); [Donaldson et al.,](#)
39 [2019](#)), groundwater fluctuations (e.g., [Clements and Denolle, 2018](#); [Illien et al., 2021](#); [Mao et al., 2022](#)), landslides (e.g.,
40 [Bièvre et al., 2018](#)), or climate-change-induced thawing (e.g., [Mordret et al., 2016](#); [Lindner et al., 2021](#)). This breadth
41 of applications makes PII a widely used methodology.

42 Processing and analysing continuous waveforms comes with multiple challenges due to the large amount of raw
43 and derived data, such as the need for efficient processing and storage strategies ([Arrowsmith et al., 2022](#)). Still today,
44 many authors use unpublished codes to produce results for later publication and interpretation making it difficult
45 for fellow researchers to reproduce or adapt the analyses. Using community codes published in the spirit of the
46 FAIR principles ([Barker et al., 2022](#)) can facilitate the reproducibility of research, exchange in the community, and
47 progress in science. Only a few software solutions exist for ambient noise seismology. Perhaps the most popular
48 among these are MSNoise ([Lecocq et al., 2014](#)) and NoisePy ([Jiang and Denolle, 2020](#)). However, as we will show
49 and discuss here, the existing software still leaves a niche to fill. For example, MSNoise is more specialised for end-
50 to-end workflows and automated monitoring solutions, lending it more towards applications in large observatories,
51 whereas, recently, NoisePy has undergone development towards cloud computing. To fill the remaining gap, we
52 introduce SeisMIC (Seismological Monitoring using Interferometric Concepts) ([Makus and Sens-Schönfelder, 2022](#)),
53 a fast, robust, flexible, and easily adapted Python tool to compute, process, and analyse dv/v . Due to these attributes,
54 SeisMIC especially excels in the analysis of campaign data, where both ease of use and flexibility are crucial.

55 **2 Modular Structure**

56 **2.1 Whom is it for? - The Philosophy behind SeisMIC**

57 As outlined above, monitoring surveys are applied to a broad spectrum of research scopes resulting in a high diver-
58 sity of requirements for research software. With that in mind, we developed SeisMIC to be flexible and adaptable to
59 user needs. As opposed to working with a black box, users work close to the source code, making it easy to develop
60 individualised workflows. Modules, submodules, or even single objects and functions of the code can also be used
61 individually. Yet, the software remains a light and fast package, in which we avoid overhead due to non-essential
62 functionality. For example, in contrast to MSNoise, we avoid heavy database management structure for continu-
63 ous observatory monitoring, resulting in a significantly faster processing (see section 2.3.2) and giving SeisMIC an
64 advantage in the analysis of campaign based data.

65 Learning to use a new code and even only determining whether a code satisfies one's need is a large time in-
66 vestment. To guarantee a fast start and a steep learning curve, we aligned SeisMIC closely with ObsPy ([Beyreuther](#)

et al., 2010), with whose syntax almost all seismologists are familiar. In addition, we host tutorials and extensive, regularly-updated documentation at <https://petermakus.github.io/SeisMIC/>. All objects, methods, and functions have documentation strings according to the Sphinx standard.

As developers, we follow the FAIR principles (Hong et al., 2022). That is, we make SeisMIC findable, accessible, interoperable, and reusable. SeisMIC is a community code with clearly communicated community standards, and users can discuss or report issues, suggest changes, or submit pull requests via GitHub. We distribute SeisMIC under the European Union Public License 1.2.

Lastly, we keep up to high standards regarding functional robustness. We test functional integrity using a combination of integral and unit tests. To date, SeisMIC has successfully been applied to a broad range of applications, such as volcanic environments (Makus et al., 2023b,a), lab-scale applications (Asnar et al., 2023), and cryoseismological analyses (Nanni et al., 2023).

2.2 Implementation

As commonplace in Python, we structure SeisMIC in a modular fashion. We divide the program into clear modules, which, in turn, are subdivided into submodules. These modules can either be used separately or connected into a workflow/pipeline, starting from data retrieval and concluding with the computation, plotting, and postprocessing of dv/v objects. We show a chart with a simplified overview of SeisMIC's modular structure in Figure 1.

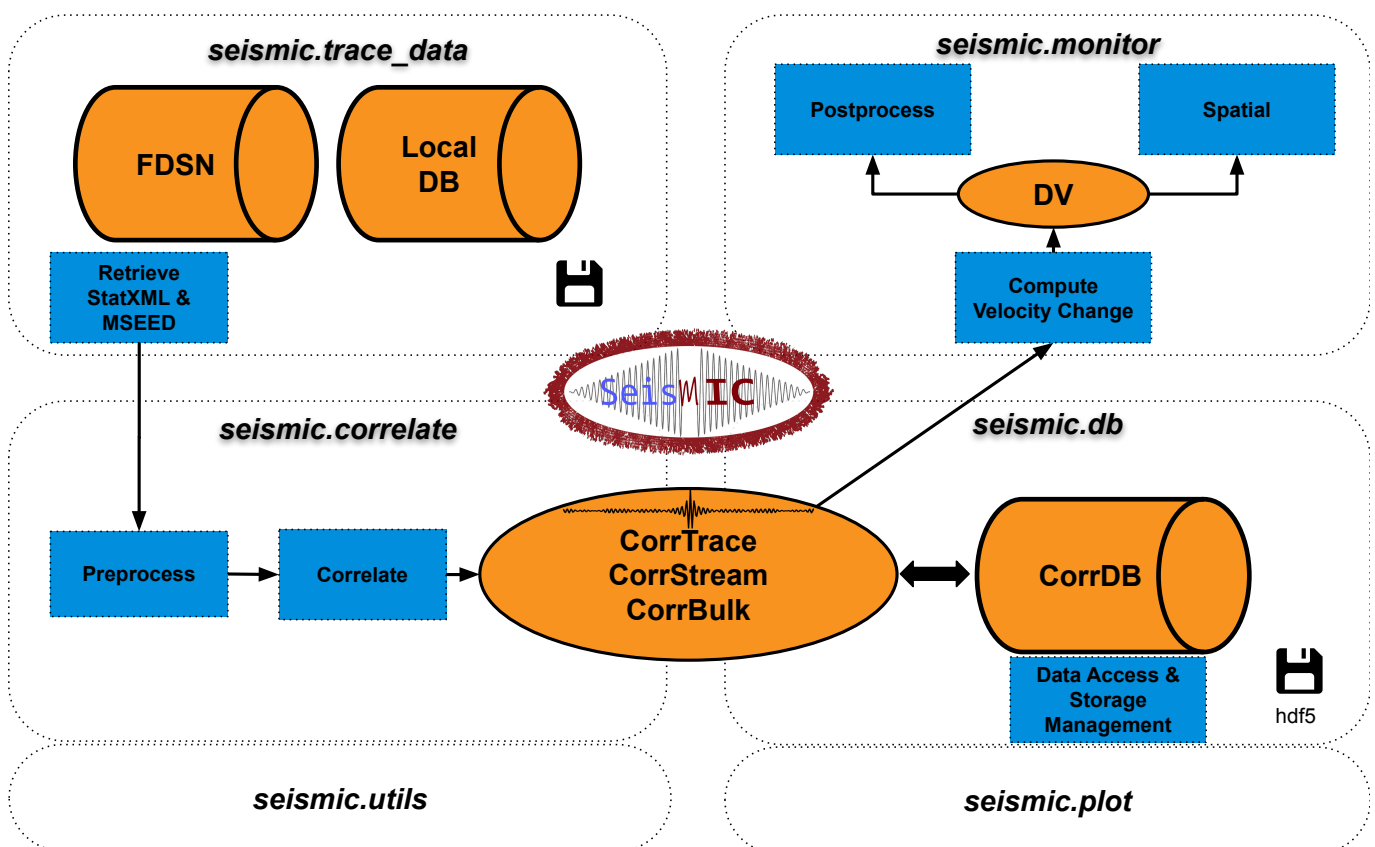


Figure 1 A flowchart summarising SeisMIC's modules and their purposes. A general workflow starts with data retrieval, continues with the computation of correlation functions, from which a velocity change time series can subsequently be estimated. We illustrate this with the example given in section 3. The depicted floppy disk marks database management modules. Operations and processes are shown in blue, whereas objects and databases are shown in orange. For the sake of simplicity, we omit non-essential objects and functions, instead, the flowchart focuses on the core processes.

As shown in Figure 1, SeisMIC consists of four main modules. `seismic.trace_data` hosts the code for reading raw waveform data and station information. Alternatively, it can request data from FDSN servers. SeisMIC handles waveform data in *miniseed* format in daily chunks, while it saves station information in *StationXML* format. Generally, station response information is only necessary if the user opts to remove the station response before correlating. However, basic station information, such as the station's geographic coordinates, is always required.

All objects and functions to preprocess waveform data and compute correlation functions (CFs) are located in `seismic.correlate`. We include commonly used preprocessing functions such as detrending, tapering, amplitude clipping, sign-bit-normalisation, or spectral whitening (Bensen et al., 2007). For a complete and up-to-date list of preprocessing functions, consult SeisMIC's documentation. Users can easily import custom processing functions into the workflow. We compute CFs by transferring traces to matrices, computing the Fourier transform, and then computing their cross-correlation in the frequency domain. Suppose we want to calculate all available correlations from a dataset of M waveforms, of which each has N samples (indices m and n , respectively). Then, the respective mathematical operations can be expressed as follows:

First, we compute the discrete Fourier transform of the matrix s containing the waveforms in the time domain:

$$S_{m,k} = \sum_{n=1}^N s_{m,n} e^{-\frac{i2\pi}{N} kn} \quad (1)$$

where $i = \sqrt{-1}$ and k is the sample index of the signal in the frequency domain. Secondly, we obtain the correlation matrix C by computing the product of the matrix with the complex conjugate of itself. We then repeat the operation M times, each time rolling the complex conjugate matrix by $j = \{1, 2, \dots, M\}$ lines:

$$C_{o,k} = S_{m,k} \overline{S_{m+j,k}} \quad (2)$$

where the bar indicates the complex conjugate and o indexes the station pair. In the described scenario, we obtain M^2 CFs, which are subsequently transferred back to the time domain:

$$C_{o,n} = \frac{1}{N} \sum_{k=1}^N C_{o,k} e^{\frac{i2\pi}{N} kn} \quad (3)$$

The CFs are then stored as special objects with attributes, plotting and post-processing methods. Finally, SeisMIC writes the CFs to a storage- and computationally-efficient *HDF5* container (Koranne, 2011).

All functionality to estimate velocity changes from the CFs resides in `seismic.monitor`. Currently, SeisMIC supports the estimation of velocity changes using the stretching technique (Sens-Schönfelder and Wegler, 2006) and we are implementing the wavelet-cross-spectrum analysis (Mao et al., 2020).

The stretching technique compares a reference correlation function \tilde{C}_n to a CF C_n^l computed from data at an arbitrary subwindow l of the total time series. Note that we omit the index o indicating the station pair since this operation is independently executed for each station pair. There are several approaches to obtaining \tilde{C} , all with their unique advantages, SeisMIC supports the use of single or multiple references (Sens-Schönfelder et al., 2014b). In SeisMIC, we implemented a grid search, in which we evaluate \tilde{C} at a new time vector $\tilde{\tau}$ stretched (or compressed)

115 with the stretching factor κ_j :

$$116 \quad \tilde{\tau}_j = \tau e^{-\kappa_j} \quad (4)$$

117 Note that we base the exponential stretching on a Taylor extension for small velocity changes. This assumption is
 118 more accurate than the more common $\tilde{\tau}_j \approx \tau(1 + \kappa_j)$ and has the advantage of yielding linearly reversible stretched
 119 functions. In the supplementary material, we provide a derivation.

120 Using our stretched time vector, we obtain a stretched reference correlation matrix with J lines, where J is the
 121 total number of tested stretch factors. Afterwards, we compute the zero-lag correlation (i.e., the normalised dot
 122 product) between each stretched reference and C^l :

$$123 \quad R_j^l = \sum_{n=1}^N \tilde{C}_n^j C_n^l \left(\sum_{n=1}^N (\tilde{C}_n^j)^2 \sum_{n=1}^N (C_n^l)^2 \right)^{-1/2} \quad (5)$$

124 The stretching factor $\kappa_j = -dv/v$ resulting in the maximum R_j^l corresponds to the negative apparent velocity
 125 change at time step l . The maximum value of R measures the velocity change estimate's stability and is often referred
 126 to as coherence. We then compute R_j^l for all time steps resulting in the similarity matrix \mathbf{R} , the final velocity change
 127 time series, and a corresponding coherence time series. Note that \mathbf{R} is usually not computed for the whole coda, but
 128 just for a user-defined subset of lag time samples. In SeisMIC, dv/v can either be jointly inverted from causal (right)
 129 and acausal (left side) or estimated from either side, which might be desirable for active source experiments or if one
 130 side of the CF exhibits a superior signal-to-noise-ratio.

131 Finally, the computed velocity change time series can be post-processed and plotted using pre-implemented or
 132 custom functions. In addition, SeisMIC can invert a set of velocity change time series from different stations onto a
 133 map using the inversion method described by [Obermann et al. \(2013\)](#). To our knowledge, SeisMIC is currently the
 134 only publicly available software that supports spatial inversion of velocity change time series.

135 The workflow steps outlined above rely entirely on well-known Python libraries, including *NumPy* ([Harris et al.,](#)
 136 [2020](#)), *SciPy* ([Virtanen et al., 2020](#)), *ObsPy* ([Beyreuther et al., 2010](#)), *Matplotlib* ([Hunter, 2007](#)), and *h5py* ([Collette et al.,](#)
 137 [2020](#)). To ensure the best stability, we only utilise the most well-maintained projects and keep the number of de-
 138 pendencies to a minimum. Some of SeisMIC's core functionalities are based on the MIIC software project ([Sens-
 139 Schönfelder et al., 2014a](#)). SeisMIC's latest beta version 0.5.3 is compatible with Python 3.10 and 3.11.

140 **2.2.1 Data Formats and Standards**

141 At the time of writing, there are no established standards for data handling in ambient noise seismology that would
 142 facilitate the exchange of correlation functions and subsequent processing with different tools. In the seismological
 143 community, excellent examples of well-designed data representations that developed into quasi-standards are the
 144 *ObsPy* ([Beyreuther et al., 2010](#)) trace and stream classes for waveform data and the inventories for station metadata.
 145 Such successful representations require some core attributes:

- 146 1. Uniformity: Various datasets have the same set of attributes, making them directly comparable.
- 147 2. Easy and flexible I/O (i.e., input/output), where data can be read, modified and stored later. Reading and writing

operations are fast and easy. Modifications can be stored safely.

3. **Interoperability:** Data can easily be imported and exported into broadly used applications or libraries, facilitating data exchange.

4. **Integrity:** The data format must contain all information required for later processing, analysis, or cataloguing. No crucial information should be lost.

With SeisMIC, we suggest a representation of noise correlation functions implementing these attributes. For correlation functions, we base our data representation on the successful ObsPy streams and traces by introducing the `CorrTrace` and `CorrStream` classes that incorporate the specific requirements of CFs to ensure uniformity and integrity.

For the storage of CFs, the seismological standard for waveform data, MiniSEED, is not appropriate since it does not allow for the storage of the required meta information. The solution provided in SeisMIC stores the data itself in the form of a NumPy array complemented with a header containing information about the recording and correlation computation, such as sample rate, start and duration of the correlated time windows, minimum and maximum lag times, seed identifiers of the used stations, and coordinates of these stations. We show an extract of the header fields for an exemplary dataset in Table 1. `CorrTrace` headers also contain information about executed processing steps, such as filtering or tapering. The naming of stations follows the SEED convention. To ensure interoperability, data and header can easily be converted into NumPy arrays and Python dictionaries, respectively. The objects come with processing and plotting methods. As outlined above, SeisMIC saves `CorrStreams` in hdf5 containers, from which they can later be read, modified, and saved again.

Table 1 Extraction from the header of a correlation function computed in section 3.

Field name	Value	Explanation
network	X9-X9	SEED network codes, dash-separated
station	IR1-IR1	SEED station codes, dash-separated
channel	HHE-HHE	SEED channel codes, dash-separated
location	-	SEED location codes, dash-separated (may be empty)
corr_start	2016-01-25T01...	UTC start time of the correlated traces
corr_end	2016-02-25T01...	UTC end time of the correlated traces
start_lag	-25.0	computed start lag in seconds
⋮	⋮	⋮

2.3 Benchmark and Performance

In ambient noise seismology, it is not uncommon to work with data volumes in the order of terabytes. We address the arising computational and storage challenges with efficient and high-performance computing (HPC) compatible code design. To this end, SeisMIC enables parallel computing of correlations, velocity change estimates and spatial inversions, where the computation of CFs is the most expensive operation by a large margin. We implement parallel computing using `mpi4py` (Dalcin and Fang, 2021), which relies on the message passing interface (MPI). In contrast to other Python multi-threading solutions, MPI-based solutions work seamlessly on high-performance computing (HPC) and cluster solutions.

In SeisMIC, the computationally most expensive parts of the workflow described in section 2.2 are the calculation of correlation functions, the associated preprocessing, and the estimation of the final velocity change time series. Therefore, an effective parallelisation scheme matters the most in these steps. For users, it is also important to understand how memory requirements scale. For the computation of CFs and the preprocessing of raw data, each core reads different raw data in chunks of equal length (see Listing 3 for details). Subsequently, the same core performs the preprocessing. For the cross-correlation operation, each core is responsible for a different component combination. This implementation makes the RAM usage practically independent of the number of cores used. Thus, RAM usage will mainly depend on the length of the raw data chunks read in each step (i.e., a smaller read length will lead to lower memory usage) and its sampling rate (i.e., a lower sampling rate will lead to lower memory usage). Resulting CFs are written to h5 files immediately after correlation or stacking and the memory is freed. In contrast, SeisMIC computes the final dv/v estimate with "1-core per component combination". Here, a single core loads all available CFs for one component combination and executes the stretching algorithm and the associated processing. Therefore, for the final dv/v calculation, the memory requirement scales with the number of employed cores.

2.3.1 Multicore Scaling

To test how SeisMIC's computational performance scales with the number of used threads, we compute autocorrelations from three component data on a single cluster node featuring an Intel Cascadelake CPU structure that is equipped with 2 CPU sockets, each holding 20 physical cores that can each execute two threads in parallel. For our test, we compute CFs from 30 days of waveform data. SeisMIC reads daily chunks of miniseed files, which it subsequently decimates, here to a sampling rate of 25 Hz, after imposing an anti-alias filter. The daily waveforms are then detrended, tapered, and filtered with a pass band between 0.01 and 12 Hz. The data is then sliced into hourly traces, which are again linearly detrended, filtered between 2 and 8 Hz, and clipped if the amplitude exceeds a threshold of 2.5 times its standard deviation. Then, SeisMIC computes hourly CFs in the frequency domain and saves them in a customised HDF5 container after performing an inverse Fourier transform. We provide the *YAML* file containing the processing parameters in the supplementary material. We execute this operation using 1, 2, 4, 8, 16, 32, and 64 threads for data from 1, 2, 4, and 8 stations (i.e., 3, 6, 12, and 24 channels and component combinations). For each configuration, we repeat the computation ten times.

Figure 2 shows the mean processing time and standard deviation over the ten operations per unique $n_{threads}$ - $n_{stations}$ -combination. We normalise the processing times by the time required for $n_{threads} = 1$ and $n_{stations} = 1$. While $n_{threads} \leq n_{channels}$, where, in our case, $n_{channels} = 3n_{stations}$, the processing time scales close to linearly with the number of used threads, indicating an excellent parallel computing performance. As most of the parallel processing in SeisMIC works on a one-core-per-channel basis, only very little increase can be expected beyond this threshold. Indeed, for $n_{channels} < n_{threads}$, the code reaches a performance plateau. From here on, the processing time increases with a further increase of $n_{threads}$, probably due to MPI's communication overhead. Based on the shown results, we would discourage hyperthreading (i.e., using more threads than available physical cores), which leads to a significant performance drop. Generally, one should not employ more threads than the total number of available channels for the computation of correlation functions or the total number of channel combinations for the dv/v estimation.

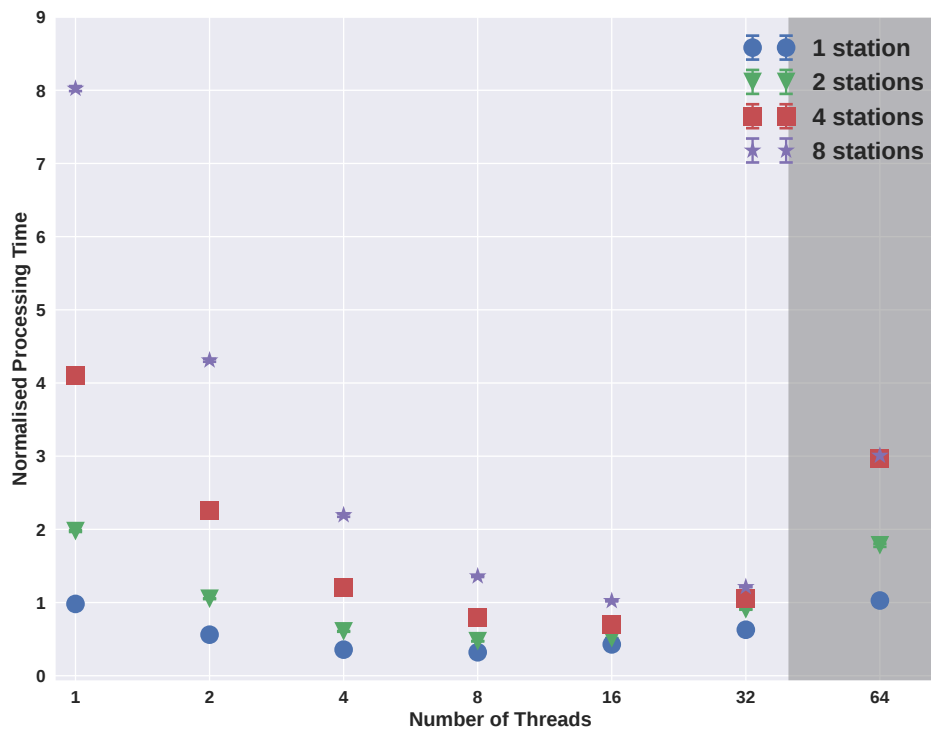


Figure 2 Multi-core scaling properties of SeisMIC. We show compute times for auto-correlations as a function of number of three-component datasets and number of parallel processing threads. The data points correspond to the mean processing time and the error bars to its standard deviation for ten operations (mostly too small to be visible). The processing times are normalised by the time needed to compute the correlations for one station using only one thread. The shaded area marks the area where the number of threads exceeds the number of physical cores, 40, i.e., the area where hyperthreading is employed.

2.3.2 Comparison with MSNoise

To analyse how SeisMIC's processing speed compares to the latest release of MSNoise (Lecocq et al., 2014), 1.6.3, we choose to calculate cross-correlations, which is the most expensive operation in a standard workflow, taking up more than 95% of the total compute time. In this benchmark, we retrieve hourly cross-correlations for 14 days of raw waveform data between eight 3-component broadband seismometers sampling at 100 Hz. We set the preprocessing to be identical for both programs. First, the data are decimated to 25 Hz. Subsequently, we detrend, taper, and band-pass filter the data between 2 and 4 Hz. Before computing the CFs, we apply one-bit normalisation and spectral whitening. We do not remove the instrument response. Note, however, that both MSNoise and SeisMIC execute the response removal using ObsPy (Beyreuther et al., 2010) and will therefore take the same amount of compute time and resources. Finally, we save the hourly CFs and daily CF stacks for all six unique component combinations with a length of 50 seconds. We perform the benchmark on the same Intel-Cascadelake-based node that we use in section 2.3.1.

We show the processing times required by MSNoise and SeisMIC for the outlined operation as a function of employed threads in Figure 3. Despite having received a significant performance boost with the update to version 1.6.x, MSNoise still needs about five times as long and thrice as much random access memory (RAM) as SeisMIC to execute the cross-correlation workflow, putting SeisMIC at a similar efficiency level as NoisePy (see Jiang and Denolle, 2020). In addition, SeisMIC offers a broader range of preprocessing options than NoisePy or MSNoise. MSNoise creates one minised file per CF, resulting in less complex writing operations, which are more evenly distributed across the cores. For this benchmark, this translates to a slightly better scaling between the number of cores and the computational

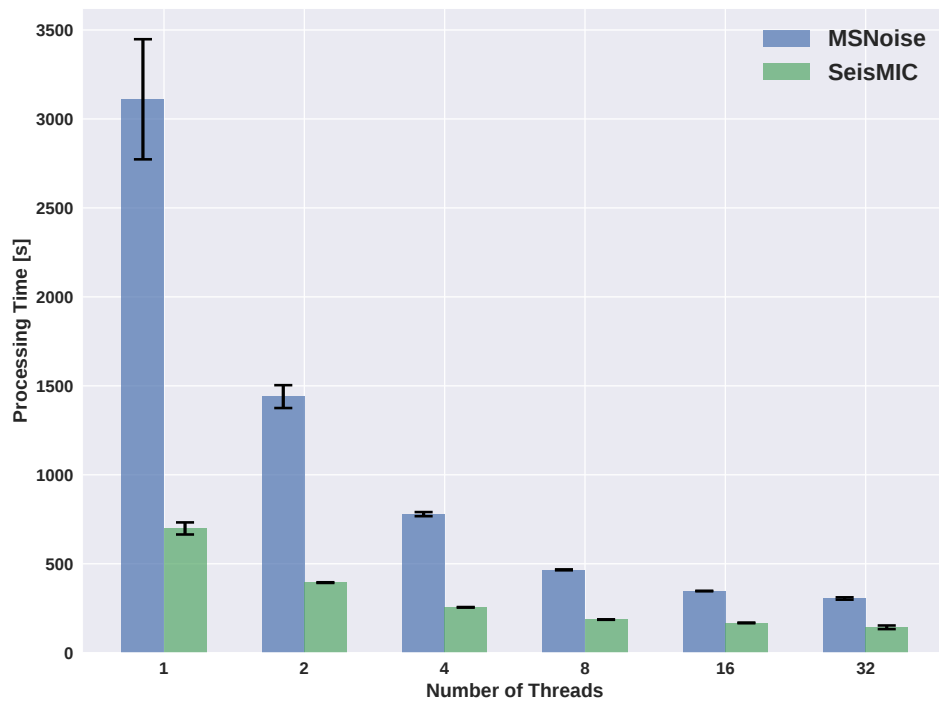


Figure 3 Compute times for a cross-correlation workflow for all six unique component combinations between eight seismic stations using MSNoise 1.6.3 (Lecocq et al., 2014) and SeisMIC 0.5.3. The height of the bars indicates the mean processing time over five iterations with the error bars representing the standard deviation. For hardware information and the exact parametrisation of the workflows, consult the text body.

time but also in a high number of files, which can be undesirable for large datasets. SeisMIC, on the other hand, creates one file per component combination. In every case, MSNoise remains more than twice as slow as SeisMIC. Note that the shown times do not include the time that MSNoise takes to set up a database and scan new data, which can take a significant amount of time, whereas these operations are practically instantaneous in SeisMIC.

While the presented results are encouraging, we remark that we could decrease compute times even further by exploiting the potential of modern graphic processing units (GPUs), which can correlate ambient seismic noise with high efficiency (Clements and Denolle, 2021; Wu et al., 2022). Implementing such algorithms belongs to the intermediate-term goals of SeisMIC’s development.

3 A Practical Example of a Workflow: From Raw Waveform Data to a Velocity Change Time Series

In this section, we demonstrate how to obtain a dv/v time series using a minimal workflow in SeisMIC. In the supplementary material, we provide two Jupyter notebooks containing the source code used for this workflow. The exemplary data are recorded by station X9.IR1 around the date of the M7.2 Zhupanov earthquake in Kamchatka, Russia. In the following, we investigate the impact of the event on the seismic velocity in the station’s vicinity. A discussion of the result lies beyond the scope of this technical paper and has already been performed by Makus et al. (2023b). We conducted this analysis using SeisMIC’s implemented workflow, which is parametrised using a simple *YAML* file (see supplementary material). In the following, we will take a step-by-step tour through said workflow and provide some minimal code examples. For further examples, we advise the reader to consult SeisMIC’s documentation and our GitHub page.

3.1 Data Retrieval

To start, we download data from an FDSN-compatible server. In our case, we download data from station X9.IR1, available over the GEOFON FDSN service (Quinteros et al., 2021). For conciseness, we restrict this example to 11 days of data from 25 January to 5 February 2016. In section 2.3, we show how SeisMIC performs when confronted to larger datasets recorded on several stations and how compute time scales when employing multiple cores. Our exemplary time window comprises the 28 January Zhupanov earthquake, whose coseismic velocity drop we want to investigate. In SeisMIC, we can initiate the data download using the `Store_Client` class and its method `download_waveforms_mdl`:

Listing 1 Downloading data using SeisMIC

```

256 from obspy import UTCDateTime
257
258 from seismic.trace_data.waveform import Store_Client
259
260 starttime = UTCDateTime(2016, 1, 25)
261 endtime = UTCDateTime(2016, 2, 5)
262
263 # Decide where data are stored
264 sc = Store_Client('GEOFON', '/path/to/project', read_only=False)
265 sc.download_waveforms_mdl(
266     starttime, endtime, clients=['GEOFON'], network='X9',
267     station='IR1', location='*', channel='HHE')

```

Under the hood, this will initiate ObsPy's (Beyreuther et al., 2010) `MassDownloader` to download continuous waveform data from the specified station if not already present locally. Here, we will compute autocorrelations using only the east component of the seismogram. We can use SeisMIC to get a first idea of the spectral content of our waveform and to investigate in which frequency bands we might find stable noise sources suitable for PII. We show a spectrogram computed using Welch windows (see, e.g., Barbe et al., 2010) as implemented in SeisMIC in Figure 4.

3.2 Computing Autocorrelations

After downloading the waveforms, we can correlate them to obtain CFs. When computing correlations, we have ample preprocessing options, which, for brevity, we will not discuss here in detail. Most fundamentally, we must set the correlation length, `corr_len`, (i.e., the duration of the time windows to be correlated), the increment between these time windows, `corr_inc`, the correlation method (in our case, autocorrelation), and the frequency window to be filtered. The user defines all options in the `YAML` file, but they can also provide parameters in a Python dictionary. For this example, we choose a correlation length of one hour and a frequency band between 2 and 4 Hz. In SeisMIC, the `Correlator` class handles the correlation workflow.

Listing 2 Downloading data using SeisMIC

```

281 from seismic.correlate.correlate import Correlator
282
283 # sc is the previously initiated Store_Client
284 c = Correlator(sc, options='path/to/params.YAML')

```

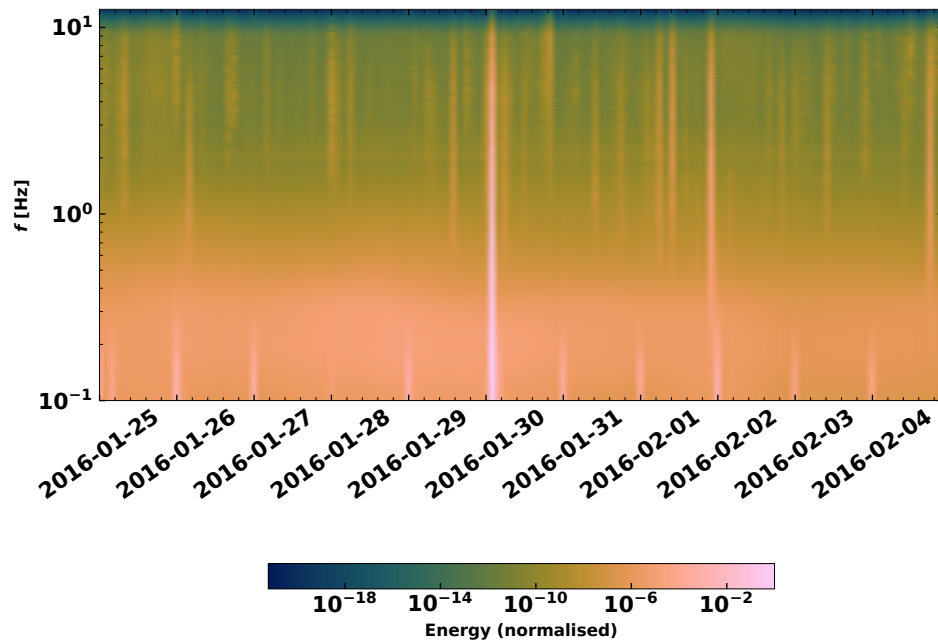


Figure 4 Time dependent spectrogram of the raw waveform at X9.IR1. We compute the spectrogram after removing the instrument response using 2 hours Welch windows. Note the energy spike caused by the Zhupanov earthquake. The energy amplitude is normalised by its maximum.

```
285 st = c.pxcorr()
```

286 To illustrate the syntax of the parameter file, we show an extract of it below. Note that the keys `preProcessing`,
 287 `TDpreProcessing`, and `FDpreProcessing` can also import custom, external functions as long as input arguments
 288 and return objects follow a predefined syntax.

Listing 3 params.YAML

```
289 ...
290 read_start : '2016-01-25 00:00:01.0'
291 read_end   : '2016-02-05 00:00:00.0'
292 sampling_rate : 25
293 remove_response : False
294 combination_method : 'autoComponents'
295 preProcessing : [
296     {'function': 'seismic.correlate.preprocessing_stream.detrend_st',
297      'args': {'type': 'linear'}},
298     {'function': 'seismic.correlate.preprocessing_stream.cos_taper_st',
299      'args': {'taper_len': 100,
300              'lossless': True}},
301     {'function': 'seismic.correlate.preprocessing_stream.stream_filter',
302      'args': {'ftype': 'bandpass',
303              'filter_option': {'freqmin': 0.01, 'freqmax': 12.49}}}]
304 subdivision:
305     corr_inc : 3600
306     corr_len : 3600
307     ...
```

```

308 corr_args : {'TDpreProcessing':[
309     {'function':'seismic.correlate.preprocessing_td.detrend',
310      'args':{'type':'linear'}},
311     {'function':'seismic.correlate.preprocessing_td.TDfilter',
312      'args':{'type':'bandpass','freqmin':2,'freqmax':4}},
313 ],
314  'lengthToSave':25,
315  'center_correlation':True,
316  'normalize_correlation':True,
317  ...
318  }
319  ...

```

Its `pxcorr` method will internally handle preprocessing and correlation. It will also initiate MPI to enable parallel processing. In Figure 5, we plotted the CFs using SeisMIC's plotting tools. Due to the high noise level in the chosen time window and frequency band, a well-defined coda emerges from the CFs (see Makus et al., 2023b, for details).

3.3 Waveform Coherence

For a first assessment of which frequency bands are well-suited for a velocity change analysis, we can use a spectrogram like the one we show in Figure 4. Additionally, one can use SeisMIC's waveform coherence function. The waveform coherence corresponds to the averaged zero-lag cross-correlation between a reference CF and CFs at time t (Steinmann et al., 2021). In Figure 6, we show the waveform coherence for our exemplary dataset computed between hourly CFs and the average CF as a reference. We determine the coherence for 5s long lapse-time windows and one-octave-wide frequency bands jointly for positive (causal) and negative (acausal) lag times. SeisMIC computes waveform coherence using the `Monitor` class and its `compute_waveform_coherence_bulk()` method (see supplementary material).

Figure 6 leads us to infer a high stability and energy content between 0.5 and 4 Hz. The coherence remains high until late lag times, e.g. for 3 Hz centre frequency, up to 75 periods. From this, we infer a highly scattering medium paired with a high energy content in this frequency band originating from the volcanic system (see Makus et al., 2023b). Therefore, we henceforth focus on the analysis of dv/v between 2 and 4 Hz.

3.4 Computing Velocity Changes Using the Stretching Method

Using the procedure theoretically outlined in section 2.2, we can estimate the evolution of the seismic velocity in the study period. Like previously, the parametrisation is handled over the `YAML` file (see supplementary material). Before computing dv/v , we smooth the one-hour CFs with a 4-hour long Hanning window. As reference CF, we use the mean of all CFs. Then, we compute dv/v for lag times between 3.5 s and 12 s simultaneously from the causal and acausal parts of the coda. We plot the resulting velocity change time series using one of SeisMIC's standard plotting templates in Figure 7.

Even though we do not focus on data interpretation in this article, we should take a brief look at the presented results. Most notably, we identify a clear velocity drop coinciding with the regional M7.2 Zhupanov earthquake. Interestingly, the resolution of the dv/v time series is high enough to identify a diurnal cycle that could be caused by

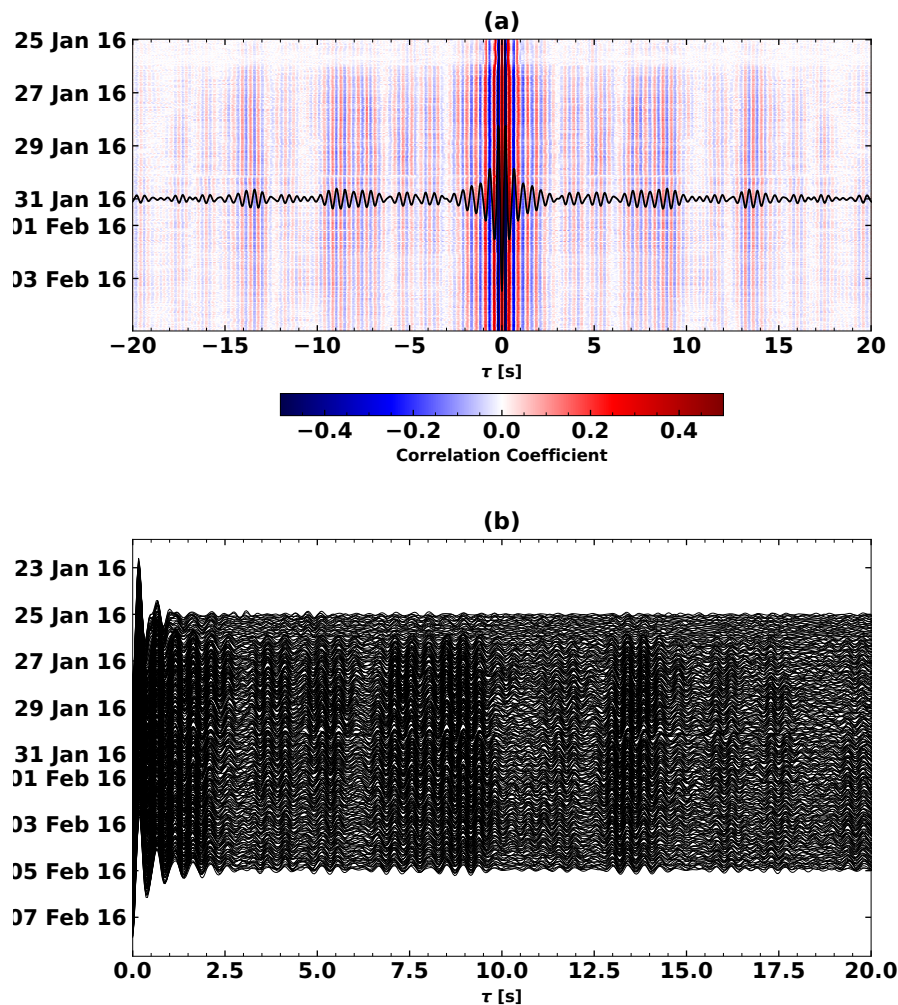


Figure 5 Hourly autocorrelations of ambient noise recorded by the east component of X9.IR1. This plot showcases two styles to plot correlations in SeisMIC. **(a)** Autocorrelations plotted as a colour image. The colours scale with the amplitude of the correlation. We superimpose the average of all shown autocorrelations on top of the heatmap. **(b)** Autocorrelations plotted as a section plot. In this plot, each hourly CF corresponds to one curve. Here, we only show the causal side of the CF.

air temperature and pressure variations, for example, observed by Wang et al. (2020), or might be due to lunar and solar tides as reported by Yamamura et al. (2003) and Sens-Schönfelder and Eulenfeld (2019). Lastly, we note that the correlation coefficient is significantly lower before 26 January 2016. We link this observation to a transient change in the wavefield as described by Makus et al. (2023b) and Steinmann et al. (2023).

3.5 Spatial Imaging of Velocity Changes

Velocity change estimates like the one presented in Figure 7 show dv/v as a function of time but do not directly yield insight into the spatial distribution of these velocity changes. Coda waves, as used in PII, sample the medium at a high spatial extent. While this allows to detect distributed weak velocity changes or changes located away from the path of direct waves, it prevents a simple inference of the affected location along a ray path or Fresnel volume. The affected location can, however, be estimated using sensitivity kernels that describe the time-dependent energy distribution

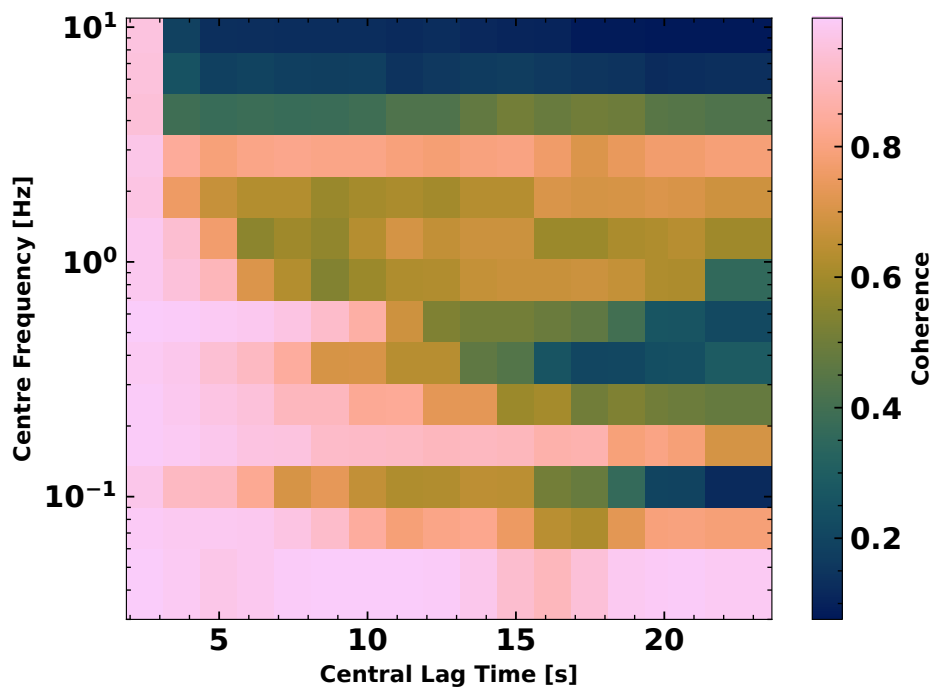


Figure 6 The waveform coherence as a function of lag time and frequency for the dataset from station X9.IR1 and channel HHE. For details, consult the text body.

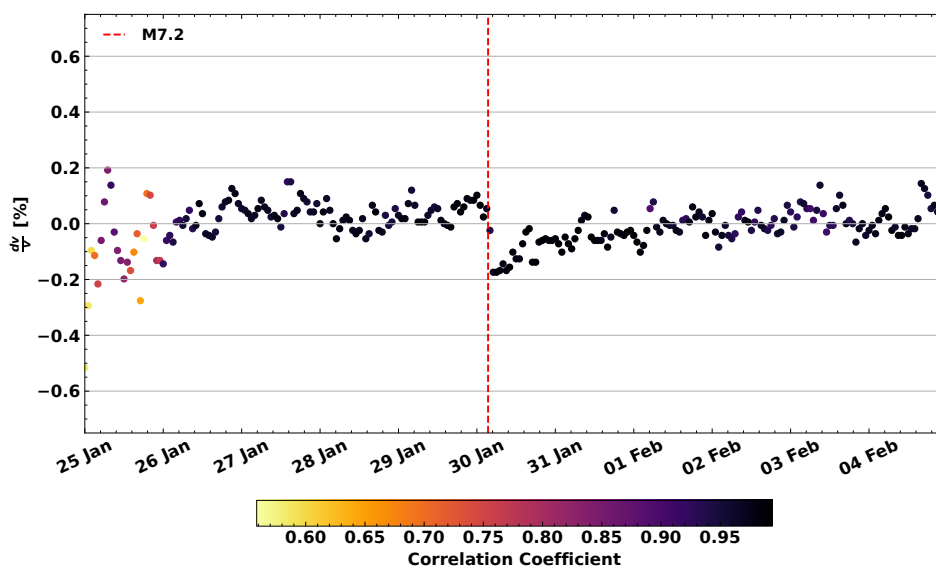


Figure 7 Velocity change time series estimated from the CFs shown in Figure 5. The increment between each data point is one hour and the shown dv/v is derived from CFs that are smoothed over 4 hours. The points' colour scales with the correlation coefficient (coherence) between the stretched CF and the reference CF. We plotted the origin time of the M7.2 Zhupanov earthquake, which occurred on 28 January 2016, as a vertical red line. An obvious velocity drop coinciding with the event can be identified. A subsequent recovery and more subtle differences in seismic velocity between day- and nighttime are visible.

356 of the wavefield for a statistically uniform medium. For a theoretical derivation of the sensitivity kernels based on
 357 the Radiative Transfer Theory, refer to Mayor et al. (2014), Margerin et al. (2016), and Zhang et al. (2022).

358 In SeisMIC, we implemented a simplified approach relying on sensitivity kernels derived from an approximate
 359 solution of the Boltzmann equation for a homogeneous medium (Paasschens, 1997) describing isotropic scattering
 360 of acoustic waves. Using these sensitivity kernels and a linearised inversion scheme proposed by Obermann et al.
 361 (2013), we can map a 2-dimensional distribution of dv/v at a fixed time t_i resulting in $dv/v(t_i, x, y)$.

362 In SeisMIC, the module `seismic.monitor.spatial` contains the necessary functions for the outlined approach.
363 To illustrate the procedure and make our example easily adaptable and reproducible, we create a synthetic velocity-
364 change model, which we then forward model onto a random station configuration. After adding noise to the synthetic
365 data, we try to recover the initial model using the inverse algorithm. In detail, we proceed as follows: First, we create
366 a synthetic velocity change model with an extent of $40 \text{ km} \times 40 \text{ km}$ and a spatial resolution of 1 km (Figures 8 (b) and
367 (d)). The background medium has a homogeneous velocity of $3 \frac{\text{km}}{\text{s}}$ and a transport mean free path l_0 of 30 km. Then,
368 we place an arbitrary number of stations on random positions along the grid. Using sensitivity kernels of cross- and
369 autocorrelations, we solve the forward problem to compute dv/v , as it would be obtained from the CFs in the presence
370 of the spatial velocity variations. The sensitivity kernels are computed for lapse time windows between 14 and 34 s.
371 To the dv/v values, we add random noise. This noise follows a Gaussian distribution around 0% velocity change with
372 a standard deviation of 0.1%. Finally, we invert for the synthetic model employing the damped linearised inversion
373 (Tarantola and Valette, 1982). We show the results of this inversion in Figures 8 (a) and (c) for 4 and 32 stations,
374 respectively. There, we also indicate the used damping parameters. The optimal damping parameters minimise
375 both the misfit between the initial and the retrieved model and the model complexity and can be found using the
376 L-curve criterion, as discussed by Obermann et al. (2013). This inversion relies on two damping parameters, the
377 correlation length λ determining how strongly related neighbouring grid cells are and the model variance σ_m that
378 the model may assume.

379 The results demonstrate that increasing the number of stations is the most powerful tool to decrease the misfit
380 between the inversion result and the input model. While the geometry of the synthetic model is poorly retrieved for
381 a configuration using only four stations, we can reproduce the model quite accurately with 32 stations.

382 The supplementary material contains a Jupyter notebook to reproduce or modify these results with an arbitrary
383 number of stations, velocity change model, and damping parameters. We also include options to invert for dv/v
384 only utilising data from auto- or cross-correlations and using sensitivity kernels from split coda windows (i.e., with
385 lapse time windows sliced into narrow sub-windows). In the supplement, we show results that exploit these options.
386 Based on these, we argue that adding dv/v information from auto- and cross-correlations, improves the accuracy of
387 the result notably, whereas splitting the coda yields only minor improvements.

388 4 Conclusion and Outlook

389 We presented SeisMIC, a software to estimate changes in the seismic propagation velocity from continuous records
390 of seismic ambient noise. SeisMIC contains functionalities for the end-to-end processing of velocity-change time
391 series, including data retrieval, the computation of correlation functions, calculating velocity change time series
392 using the stretching method, and postprocessing as well as inverting dv/v time series onto a spatial grid. While
393 these functions can be part of a workflow, they are also intended to be used separately and can easily be altered
394 and adapted to individual processes. In SeisMIC, we implement a new data format for correlation functions, which
395 provides uniformity, flexibility, interoperability, and integrity. Thereby, we hope to foster a broader discussion in the
396 community regarding data standards, which, we believe, would aid data exchange, efficiency, and reproducibility of
397 ambient noise studies.

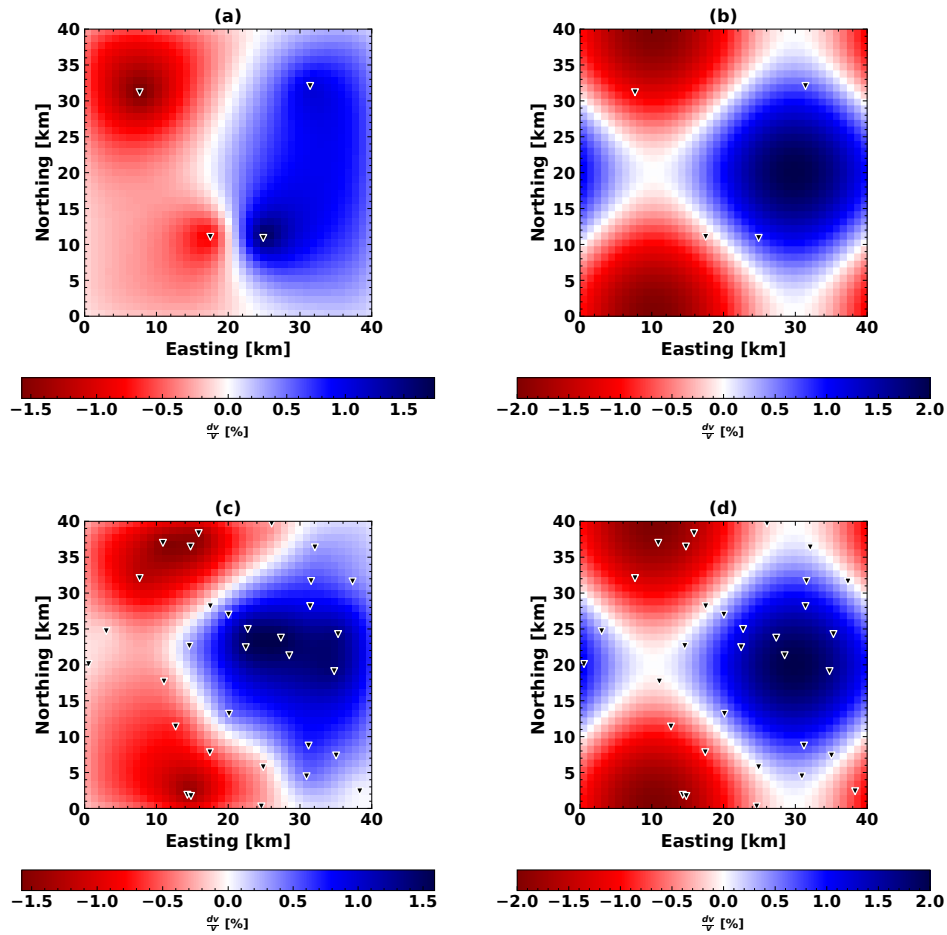


Figure 8 Two examples of the spatial inversion using different parametrisations and station configurations. **(a)** Result of the spatial inversion algorithm using four stations, a model variance $\sigma_m = 0.1 \frac{\text{km}}{\text{km}^2}$, and a correlation length $\lambda = 2$ km. **(b)** The synthetic velocity model and station configuration used to obtain (a). **(c)** Result of the spatial inversion algorithm using 32 stations, $\sigma_m = 0.01 \frac{\text{km}}{\text{km}^2}$, and $\lambda = 2$ km. **(d)** The synthetic velocity model and station configuration used to obtain (c). For an exhaustive description of the parametrisation and the inversion steps, consult the text body.

In the near future, we will release versions capable of estimating dv/v employing algorithms other than the stretching method, like the wavelet-cross-spectrum analysis (Mao et al., 2020). Other future milestones include exploiting the computational power of GPUs to decrease the compute time of noise correlations even further and adding solutions that automatically update correlation function databases.

SeisMIC complements existing software to process ambient noise. Highlights are its broad functionality, high efficiency, and versatility applicable to local small-scale studies on a laptop computer as well as surveys using large-N arrays processed on computer clusters. SeisMIC is available on GitHub as a well-documented and regularly maintained open-source software.

Acknowledgements

We thank Luc Illien, Ugo Nanni, Jannes Münchmeyer, Marine Denolle, Charlotte Bruland, Tuo Zhang, and Raphael De Plaen for discussions that helped improving this software. This work was supported by the DFG grant SE1844/12-1. We are grateful for comments and suggestions towards improvement of this work by Laura Ermert and two anonymous reviewers.

411 **Data and code availability**

412 This manuscript is distributed with a supporting information in PDF format. Aside from the supporting document,
413 we provide Jupyter notebooks, computing scripts, and the main program "SeisMIC" as a digital supplement. For
414 SeisMIC, however, we strongly encourage the reader to obtain the code's latest version, for example, from GitHub.
415 The digital supplement includes SeisMIC 0.5.3 and is available at <https://doi.org/10.5281/zenodo.8283683>.

416 The SeisMIC data from the KISS experiment (Shapiro et al., 2017) used in section 3 can be obtained from the GE-
417 OFON webservice (Quinteros et al., 2021). For the benchmarks in section 2.3, we used data from the Saxony Network
418 (University of Leipzig, 2001) available from the EIDA FDSN service (Strollo et al., 2021).

419 **Competing interests**

420 The authors do not declare any competing interests.

421 **References**

- 422 Arrowsmith, S. J., Trugman, D. T., MacCarthy, J., Bergen, K. J., Lumley, D., and Magnani, M. B. Big Data Seismology. *Reviews of Geophysics*,
423 60(2):e2021RG000769, 2022. doi: 10.1029/2021RG000769.
- 424 Asnar, M., Sens-Schönfelder, C., Bonnelye, A., and Dresen, G. Non-Classical, Non-Linear Elasticity in Rocks: Experiments in a Triaxial Cell
425 with Pore Pressure Control. Technical Report EGU23-8050, Copernicus Meetings, Feb. 2023.
- 426 Barbe, K., Pintelon, R., and Schoukens, J. Welch Method Revisited: Nonparametric Power Spectrum Estimation Via Circular Overlap. *IEEE*
427 *Transactions on Signal Processing*, 58(2):553–565, Feb. 2010. doi: 10.1109/TSP.2009.2031724.
- 428 Barker, M., Chue Hong, N. P., Katz, D. S., Lamprecht, A.-L., Martinez-Ortiz, C., Psomopoulos, F., Harrow, J., Castro, L. J., Gruenpeter,
429 M., Martinez, P. A., and Honeyman, T. Introducing the FAIR Principles for Research Software. *Scientific Data*, 9(1):622, Oct. 2022.
430 doi: 10.1038/s41597-022-01710-x.
- 431 Bensen, G. D., Ritzwoller, M. H., Barmin, M. P., Levshin, A. L., Lin, F., Moschetti, M. P., Shapiro, N. M., and Yang, Y. Processing Seismic Ambient
432 Noise Data to Obtain Reliable Broad-Band Surface Wave Dispersion Measurements. *Geophysical Journal International*, 169(3):1239–1260,
433 2007. doi: 10.1111/j.1365-246X.2007.03374.x.
- 434 Beyreuther, M., Barsch, R., Krischer, L., Megies, T., Behr, Y., and Wassermann, J. ObsPy: A Python Toolbox for Seismology. *Seismological*
435 *Research Letters*, 81(3):530–533, May 2010. doi: 10.1785/gssrl.81.3.530.
- 436 Bièvre, G., Franz, M., Larose, E., Carrière, S., Jongmans, D., and Jaboyedoff, M. Influence of Environmental Parameters on the Seis-
437 mic Velocity Changes in a Clayey Mudflow (Pont-Bourquin Landslide, Switzerland). *Engineering Geology*, 245:248–257, Nov. 2018.
438 doi: 10.1016/j.enggeo.2018.08.013.
- 439 Brenguier, F., Campillo, M., Hadziioannou, C., Shapiro, N. M., Nadeau, R. M., and Larose, E. Postseismic Relaxation Along
440 the San Andreas Fault at Parkfield from Continuous Seismological Observations. *Science*, 321(5895):1478–1481, Sept. 2008.
441 doi: 10.1126/science.1160943.
- 442 Clements, T. and Denolle, M. A. Tracking Groundwater Levels Using the Ambient Seismic Field. *Geophysical Research Letters*, 45(13):6459–
443 6465, 2018. doi: 10.1029/2018GL077706.
- 444 Clements, T. and Denolle, M. A. SeisNoise.Jl: Ambient Seismic Noise Cross Correlation on the CPU and GPU in Julia. *Seismological Research*
445 *Letters*, 92(1):517–527, 2021. doi: 10.1785/0220200192.

- 446 Clymer, R. W. and McEvelly, T. V. Travel-Time Monitoring with Vibroseis*. *Bulletin of the Seismological Society of America*, 71(6):1903–1927,
447 Dec. 1981. doi: 10.1785/BSSA0710061903.
- 448 Collette, A., Kluyver, T., Caswell, T. A., Tocknell, J., Kieffer, J., Scopatz, A., Dale, D., Chen, Jelenak, A., payno, juliagarriga, VINCENT, T., Sciarelli,
449 P., Valls, V., Kofoed Pedersen, U., jakirkham, Raspaud, M., Parsons, A., Abbasi, H., Readey, J., Paramonov, A., Chan, L., jialin, Danilevski, C.,
450 Feng, Y., Vaillant, G. A., Teichmann, M., Brucher, M., Johnson, S. R., and Hole, L. H5py/H5py: 3.1.0. *Zenodo*, Nov. 2020. doi: 10.5281/zen-
451 odo.4250762.
- 452 Dalcin, L. and Fang, Y.-L. L. Mpi4py: Status Update After 12 Years of Development. *Computing in Science & Engineering*, 23(4):47–54, July
453 2021. doi: 10.1109/MCSE.2021.3083216.
- 454 Donaldson, C., Winder, T., Caudron, C., and White, R. S. Crustal Seismic Velocity Responds to a Magmatic Intrusion and Seasonal Loading
455 in Iceland’s Northern Volcanic Zone. *Science Advances*, 5(11):eaax6642, Nov. 2019. doi: 10.1126/sciadv.aax6642.
- 456 Harris, C. R., Millman, K. J., van der Walt, S. J., Gommers, R., Virtanen, P., Cournapeau, D., Wieser, E., Taylor, J., Berg, S., Smith, N. J., Kern,
457 R., Picus, M., Hoyer, S., van Kerkwijk, M. H., Brett, M., Haldane, A., del Río, J. F., Wiebe, M., Peterson, P., Gérard-Marchant, P., Sheppard, K.,
458 Reddy, T., Weckesser, W., Abbasi, H., Gohlke, C., and Oliphant, T. E. Array Programming with NumPy. *Nature*, 585(7825):357–362, Sept.
459 2020. doi: 10.1038/s41586-020-2649-2.
- 460 Hirose, T., Nakahara, H., and Nishimura, T. Combined Use of Repeated Active Shots and Ambient Noise to Detect Temporal Changes in
461 Seismic Velocity: Application to Sakurajima Volcano, Japan 4. *Seismology. Earth, Planets and Space*, 69(1), 2017. doi: 10.1186/s40623-
462 017-0613-7.
- 463 Hong, N. P. C., Katz, D. S., Barker, M., Lamprecht, A.-L., Martinez, C., Psomopoulos, F. E., Harrow, J., Castro, L. J., Gruenpeter, M., Mar-
464 tinez, P. A., Honeyman, T., Struck, A., Lee, A., Loewe, A., van Werkhoven, B., Garijo, D., Plomp, E., Genova, F., Shanahan, H., Hellström,
465 M., Sandström, M., Sinha, M., Kuzak, M., Herterich, P., Islam, S., Sansone, S.-A., Pollard, T., Atmojo, U. D., Williams, A., Czerniak, A.,
466 Niehues, A., Fouilloux, A. C., Desinghu, B., Goble, C., Richard, C., Gray, C., Erdmann, C., Nüst, D., Tartarini, D., Ranguelova, E., Anzt, H.,
467 Todorov, I., McNally, J., Burnett, J., Garrido-Sánchez, J., Belhajjame, K., Sesink, L., Hwang, L., Tovani-Palone, M. R., Wilkinson, M. D.,
468 Servillat, M., Liffers, M., Fox, M., Miljković, N., Lynch, N., Lavanchy, P. M., Gesing, S., Stevens, S., Cuesta, S. M., Peroni, S., Soiland-Reyes,
469 S., Bakker, T., Rabemanantsoa, T., Sochat, V., Yehudi, Y., and Wg, F. FAIR Principles for Research Software (FAIR4RS Principles). Mar. 2022.
470 doi: 10.15497/RDA00065.
- 471 Hunter, J. D. Matplotlib: A 2D Graphics Environment. *Computing in Science & Engineering*, 9(03):90–95, May 2007. doi: 10.1109/M-
472 CSE.2007.55.
- 473 Ikuta, R., Yamaoka, K., Miyakawa, K., Kunitomo, T., and Kumazawa, M. Continuous Monitoring of Propagation Velocity of Seismic Wave
474 Using ACROSS. *Geophysical Research Letters*, 29(13):5–1–5–5, 2002. doi: 10.1029/2001GL013974.
- 475 Illien, L., Andermann, C., Sens-Schönfelder, C., Cook, K. L., Baidya, K. P., Adhikari, L. B., and Hovius, N. Subsurface Moisture Regulates
476 Himalayan Groundwater Storage and Discharge. *AGU Advances*, 2(2), 2021. doi: 10.1029/2021av000398.
- 477 Jiang, C. and Denolle, M. A. Noisepy: A New High-Performance Python Tool for Ambient-Noise Seismology. *Seismological Research Letters*,
478 91(3):1853–1866, 2020. doi: 10.1785/0220190364.
- 479 Koranne, S. Hierarchical Data Format 5 : HDF5. In Koranne, S., editor, *Handbook of Open Source Tools*, pages 191–200. Springer US, Boston,
480 MA, 2011.
- 481 Lecocq, T., Caudron, C., and Brenguier, F. MSNoise, a Python Package for Monitoring Seismic Velocity Changes Using Ambient Seismic
482 Noise. *Seismological Research Letters*, 85(3):715–726, May 2014. doi: 10.1785/0220130073.
- 483 Lindner, F., Wassermann, J., and Igel, H. Seasonal Freeze-Thaw Cycles and Permafrost Degradation on Mt. Zugspitze (German/Austrian

- 484 Alps) Revealed by Single-Station Seismic Monitoring. *Geophysical Research Letters*, 48(18):1–11, 2021. doi: 10.1029/2021GL094659.
- 485 Makus, P. and Sens-Schönfelder, C. Seismological Monitoring Using Interferometric Concepts (SeisMIC). GFZ Data Services, 2022.
- 486 Makus, P., Denolle, M., Sens-Schönfelder, C., Köpfl, M., and Tilmann, F. The Complex Relationship between Seismic Velocity and Volcanic,
487 Tectonic, and Environmental Forcings Illustrated by 23 Years of Data at Mt. St. Helens. In *EGU23*. Copernicus Meetings, Feb. 2023a.
488 doi: 10.5194/egusphere-egu23-6757.
- 489 Makus, P., Sens-Schönfelder, C., Illien, L., Walter, T. R., Yates, A., and Tilmann, F. Deciphering the Whisper of Volcanoes: Monitoring Ve-
490 locity Changes at Kamchatka's Klyuchevskoy Group With Fluctuating Noise Fields. *Journal of Geophysical Research: Solid Earth*, 128(4):
491 e2022JB025738, 2023b. doi: 10.1029/2022JB025738.
- 492 Mao, S., Mordret, A., Campillo, M., Fang, H., and van der Hilst, R. D. On the Measurement of Seismic Traveltime Changes in the
493 Time–Frequency Domain with Wavelet Cross-Spectrum Analysis. *Geophysical Journal International*, 221(1):550–568, Apr. 2020.
494 doi: 10.1093/gji/ggz495.
- 495 Mao, S., Lecointre, A., van der Hilst, R. D., and Campillo, M. Space-Time Monitoring of Groundwater Fluctuations with Passive Seismic
496 Interferometry. *Nature Communications*, 13(1):4643, Aug. 2022. doi: 10.1038/s41467-022-32194-3.
- 497 Margerin, L., Planès, T., Mayor, J., and Calvet, M. Sensitivity Kernels for Coda-Wave Interferometry and Scattering Tomography: Theory and
498 Numerical Evaluation in Two-Dimensional Anisotropically Scattering Media. *Geophysical Journal International*, 204(1):650–666, Jan.
499 2016. doi: 10.1093/gji/ggv470.
- 500 Mayor, J., Margerin, L., and Calvet, M. Sensitivity of Coda Waves to Spatial Variations of Absorption and Scattering: Radiative Transfer
501 Theory and 2-D Examples. *Geophysical Journal International*, 197(2):1117–1137, May 2014. doi: 10.1093/gji/ggu046.
- 502 Minato, S., Tsuji, T., Ohmi, S., and Matsuoka, T. Monitoring Seismic Velocity Change Caused by the 2011 Tohoku-oki Earthquake Using
503 Ambient Noise Records. *Geophysical Research Letters*, 39(9), 2012. doi: 10.1029/2012GL051405.
- 504 Mordret, A., Mikesell, T. D., Harig, C., Lipovsky, B. P., and Prieto, G. A. Monitoring Southwest Greenland's Ice Sheet Melt with Ambient Seismic
505 Noise. *Science Advances*, 2(5):e1501538, May 2016. doi: 10.1126/sciadv.1501538.
- 506 Nanni, U., Pauze, T., Goulet, L., Köhler, A., Bouchayer, C., and Schuler, T. Study of the Structural and Dynamic Changes of a Surging Glacier
507 Using Seismic Observations. In *IUGG*, Berlin, July 2023.
- 508 Nishimura, T., Uchida, N., Sato, H., Ohtake, M., Tanaka, S., and Hamaguchi, H. Temporal Changes of the Crustal Structure Associated with
509 the M6.1 Earthquake on September 3, 1998, and the Volcanic Activity of Mount Iwate, Japan. *Geophysical Research Letters*, 27(2):269–272,
510 2000. doi: 10.1029/1999GL005439.
- 511 Obermann, A., Planès, T., Larose, E., and Campillo, M. Imaging Preeruptive and Coeruptive Structural and Mechanical Changes of a Volcano
512 with Ambient Seismic Noise. *Journal of Geophysical Research: Solid Earth*, 118(12):6285–6294, 2013. doi: 10.1002/2013JB010399.
- 513 Paasschens, J. C. J. Solution of the Time-Dependent Boltzmann Equation. *Physical Review E*, 56(1):1135–1141, July 1997. doi: 10.1103/Phys-
514 RevE.56.1135.
- 515 Poupinet, G., Ellsworth, W. L., and Frechet, J. Monitoring Velocity Variations in the Crust Using Earthquake Doublets: An Application to the
516 Calaveras Fault, California. *Journal of Geophysical Research: Solid Earth*, 89(B7):5719–5731, July 1984. doi: 10.1029/JB089iB07p05719.
- 517 Quinteros, J., Strollo, A., Evans, P. L., Hanka, W., Heinloo, A., Hemmleb, S., Hillmann, L., Jaeckel, K.-H., Kind, R., Saul, J., Zieke, T., and
518 Tilmann, F. The GEOFON Program in 2020. *Seismological Research Letters*, 92(3):1610–1622, Feb. 2021. doi: 10.1785/0220200415.
- 519 Sawazaki, K., Kimura, H., Shiomi, K., Uchida, N., Takagi, R., and Snieder, R. Depth-Dependence of Seismic Velocity Change Associated with
520 the 2011 Tohoku Earthquake, Japan, Revealed from Repeating Earthquake Analysis and Finite-Difference Wave Propagation Simulation.
521 *Geophysical Journal International*, 201(2):741–763, May 2015. doi: 10.1093/gji/ggv014.

- 522 Sens-Schönfelder, C. and Eulenfeld, T. Probing the in Situ Elastic Nonlinearity of Rocks with Earth Tides and Seismic Noise. *Physical Review*
523 *Letters*, 122(13):138501, Apr. 2019. doi: 10.1103/PhysRevLett.122.138501.
- 524 Sens-Schönfelder, C. and Wegler, U. Passive Image Interferometry and Seasonal Variations of Seismic Velocities at Merapi Volcano, Indone-
525 sia. *Geophysical Research Letters*, 33(21):1–5, 2006. doi: 10.1029/2006GL027797.
- 526 Sens-Schönfelder, C. and Wegler, U. Passive Image Interferometry for Monitoring Crustal Changes with Ambient Seismic Noise. *Comptes*
527 *Rendus Geoscience*, 343(8):639–651, Sept. 2011. doi: 10.1016/j.crte.2011.02.005.
- 528 Sens-Schönfelder, C., Flores-Estrella, H., Gassenmeier, M., Korn, M., Köllner, F., Milkereit, C., Niederleithinger, E., Parolai, S., Pilz, M., Pom-
529 poni, E., Schuck, A., Thiemann, K., and Völkel, J. MIIC: Monitoring and Imaging Based on Interferometric Concepts. In Weber, M. and
530 Münch, U., editors, *Tomography of the Earth's Crust: From Geophysical Sounding to Real-Time Monitoring: GEOTECHNOLOGIEN Science*
531 *Report No. 21*, Advanced Technologies in Earth Sciences, pages 43–61. Springer International Publishing, Cham, 2014a.
- 532 Sens-Schönfelder, C., Pomponi, E., and Peltier, A. Dynamics of Piton de La Fournaise Volcano Observed by Passive Image Interferometry
533 with Multiple References. *Journal of Volcanology and Geothermal Research*, 276:32–45, 2014b. doi: 10.1016/j.jvolgeores.2014.02.012.
- 534 Shapiro, N., Sens-Schönfelder, C., Lühr, B., Weber, M., Abkadyrov, I., Gordeev, E., Koulakov, I., Jakovlev, A., Kugaenko, Y., and Saltykov, V.
535 Understanding Kamchatka's Extraordinary Volcano Cluster. *Eos*, May 2017. doi: 10.1029/2017EO071351.
- 536 Snieder, R., Grêt, A., Douma, H., and Scales, J. Coda Wave Interferometry for Estimating Nonlinear Behavior in Seismic Velocity. *Science*,
537 295(5563):2253–2255, 2002. doi: 10.1126/science.1070015.
- 538 Steinmann, R., Hadziioannou, C., and Larose, E. Effect of Centimetric Freezing of the near Subsurface on Rayleigh and Love Wave Velocity
539 in Ambient Seismic Noise Correlations. *Geophysical Journal International*, 224(1):626–636, 2021. doi: 10.1093/gji/ggaa406.
- 540 Steinmann, R., Seydoux, L., Journeau, C., Shapiro, N. M., and Campillo, M. Machine Learning Analysis of Seismograms Reveals a Continuous
541 Plumbing System Evolution beneath the Klyuchevskoy Volcano in Kamchatka, Russia, June 2023.
- 542 Strollo, A., Cambaz, D., Clinton, J., Danecek, P., Evangelidis, C. P., Marmureanu, A., Ottemöller, L., Pedersen, H., Sleeman, R., Stammler,
543 K., Armbruster, D., Bienkowski, J., Boukouras, K., Evans, P. L., Fares, M., Neagoe, C., Heimers, S., Heinloo, A., Hoffmann, M., Kaestli, P.,
544 Lauciani, V., Michalek, J., Odon Muhire, E., Ozer, M., Palangeanu, L., Pardo, C., Quinteros, J., Quintiliani, M., Antonio Jara-Salvador, J.,
545 Schaeffer, J., Schloemer, A., and Triantafyllis, N. EIDA: The European Integrated Data Archive and Service Infrastructure within ORFEUS.
546 *Seismological Research Letters*, 92(3):1788–1795, Mar. 2021. doi: 10.1785/0220200413.
- 547 Tarantola, A. and Valette, B. Generalized Nonlinear Inverse Problems Solved Using the Least Squares Criterion. *Reviews of Geophysics*, 20
548 (2):219–232, 1982. doi: 10.1029/RG020i002p00219.
- 549 University of Leipzig. SXNET Saxon Seismic Network, 2001.
- 550 Virtanen, P., Gommers, R., Oliphant, T. E., Haberland, M., Reddy, T., Cournapeau, D., Burovski, E., Peterson, P., Weckesser, W., Bright, J., van
551 der Walt, S. J., Brett, M., Wilson, J., Millman, K. J., Mayorov, N., Nelson, A. R. J., Jones, E., Kern, R., Larson, E., Carey, C. J., Polat, İ., Feng,
552 Y., Moore, E. W., VanderPlas, J., Laxalde, D., Perktold, J., Cimrman, R., Henriksen, I., Quintero, E. A., Harris, C. R., Archibald, A. M., Ribeiro,
553 A. H., Pedregosa, F., and van Mulbregt, P. SciPy 1.0: Fundamental Algorithms for Scientific Computing in Python. *Nature Methods*, 17(3):
554 261–272, Mar. 2020. doi: 10.1038/s41592-019-0686-2.
- 555 Wang, B., Yang, W., Wang, W., Yang, J., Li, X., and Ye, B. Diurnal and Semidiurnal P- and S-Wave Velocity Changes Measured Using an Airgun
556 Source. *Journal of Geophysical Research: Solid Earth*, 125(1):e2019JB018218, 2020. doi: 10.1029/2019JB018218.
- 557 Wang, Q. Y., Brenguier, F., Campillo, M., Lecointre, A., Takeda, T., and Aoki, Y. Seasonal Crustal Seismic Velocity Changes Throughout Japan.
558 *Journal of Geophysical Research: Solid Earth*, 122(10):7987–8002, 2017. doi: 10.1002/2017JB014307.
- 559 Wegler, U., Lühr, B. G., Snieder, R., and Ratdomopurbo, A. Increase of Shear Wave Velocity before the 1998 Eruption of Merapi Volcano

- 560 (Indonesia). *Geophysical Research Letters*, 33(9):4–7, 2006. doi: 10.1029/2006GL025928.
- 561 Wu, C., Tan, X., Li, H., and Sun, G. An Efficient Ambient Noise Cross-Correlation Algorithm on Heterogeneous CPU-GPU Cluster.
562 In *2022 IEEE 13th International Symposium on Parallel Architectures, Algorithms and Programming (PAAP)*, pages 1–5, Nov. 2022.
563 doi: 10.1109/PAAP56126.2022.10010612.
- 564 Yamamura, K., Sano, O., Utada, H., Takei, Y., Nakao, S., and Fukao, Y. Long-Term Observation of in Situ Seismic Velocity and Attenuation.
565 *Journal of Geophysical Research: Solid Earth*, 108(B6), 2003. doi: 10.1029/2002JB002005.
- 566 Yang, W., Wang, B., Yuan, S., and Ge, H. Temporal Variation of Seismic-Wave Velocity Associated with Groundwater Level Observed by a
567 Downhole Airgun near the Xiaojiang Fault Zone. *Seismological Research Letters*, 89(3):1014–1022, Apr. 2018. doi: 10.1785/0220170282.
- 568 Zhang, H., Glasgow, M., Schmandt, B., Thelen, W. A., Moran, S. C., and Thomas, A. M. Revisiting the Depth Distribution of Seismicity be-
569 fore and after the 2004–2008 Eruption of Mount St. Helens. *Journal of Volcanology and Geothermal Research*, 430:107629, Oct. 2022.
570 doi: 10.1016/j.jvolgeores.2022.107629.

Supporting Information for "SeisMIC - an Open Source Python Toolset to Compute Velocity Changes from Ambient Seismic Noise"

Peter Makus *,^{1,2}, Christoph Sens-Schönfelder ¹

¹Helmholtz Center, German Research Center for Geosciences GFZ, Potsdam, Germany, ²Institute for Geological Sciences, Freie Universität Berlin, Berlin, Germany

1 Introduction

In this supporting information, we elaborate on the approximation of the stretching factor implemented in SeisMIC. We show a short derivation in section 2.

In section 3, we present selected results of the spatial inversion procedure to illustrate the effect of (1) subdividing the coda to obtain several independent velocity change estimates (hereafter referred to as coda splitting) and (2) adding information from autocorrelations and cross-station correlations to the analysis. To this end, we provide several examples using different station configurations and damping parameters. For a thorough discussion of the algorithm, please refer to the main manuscript. The reader can reproduce and extend the shown results using the `spatial.ipynb` Jupyter notebook provided in the digital supplement.

For the coda splitting, we split the total of the used coda window into three equally long subwindows and obtain one sensitivity kernel for each subwindow. That is when exploiting the coda splitting, we compute separate sensitivity kernels for lapse times from 14 to 20.66 s, from 20.66 s to 27.33 s, and from 27.33 s to 34 s, whereas without coda splitting, we only obtain one sensitivity kernel representing lag times from 14 s to 34 s. To all forward-modelled dv/v results, we add random noise from a Gaussian distribution with a standard deviation of only 0.05% dv/v to the predicted velocity changes to render the comparison less dependent on the noise level. Otherwise, the procedure for the spatial inversion remains identical to the one described in the main manuscript section 3.5.

Apart from this supporting document, we provide Jupyter notebooks, computing scripts, and the main program, SeisMIC 0.5.3, as a digital supplement. For SeisMIC, however, we strongly encourage the reader to obtain the code's latest version, for example, from GitHub. For details about where to retrieve these additional supplements, please refer to the *data and code availability* section in the main manuscript.

2 Derivation of the Stretching

A problem with the commonly used definition of a velocity change dv/v is that it is neither additive nor reversible, i.e. $dv/v_{A \rightarrow B} \neq -dv/v_{B \rightarrow A}$ because the reference velocity of the two measurements may be different and the commonly

*Corresponding author: makus@gfz-potsdam.de

used equation $dv/v = -dt/t$ is an approximation for small dv/v . Even though the error is small, we can reduce it further with a different definition of the velocity change. This definition is especially useful for smoothing, averaging, or otherwise manipulating velocity change time series as, in contrast to the common definition, it ensures linearity (see below).

Assuming infinite frequency (i.e., ray theory), the travel time $t(\mathbf{x})$ of a wave travelling from point \mathbf{x}_1 to \mathbf{x}_2 through any medium is given by:

$$t(\mathbf{x}) = \int_{\mathbf{x}_1}^{\mathbf{x}_2} \frac{1}{v(\mathbf{x})} d\mathbf{x} \quad (1)$$

where $v(\mathbf{x})$ is the velocity at point \mathbf{x} . If we assume a medium with a homogeneous velocity, i.e., $v(\mathbf{x}) = v$, equation 1 simplifies to:

$$t = \frac{\Delta x}{v} \quad (2)$$

where $\Delta x = \|\mathbf{x}_1 - \mathbf{x}_2\|$ is the Euclidean distance which remains constant throughout. In interferometry, we examine the case where the velocity $v(t)$ is variable with time. To quantify the change in velocity, we compare the velocity of a reference state $\tilde{v} = \Delta x / \tilde{t}$ with the velocity $v' = \Delta x / t'$ in a perturbed state. Due to the constant Δx , we obtain from equation 2:

$$\frac{\tilde{t}}{t'} = \frac{v'}{\tilde{v}} = \xi \quad (3)$$

defining the stretching factor ξ .

We seek a transformation

$$\mathcal{S}(\kappa) : \tilde{t} \mapsto t' = \frac{1}{\xi} \tilde{t}$$

that maps the original travel times \tilde{t} of the seismic waves through the unperturbed medium to the travel times t' through the perturbed medium. This transformation shall have the following property:

$$\mathcal{S}(\kappa_1)\mathcal{S}(\kappa_2) = \mathcal{S}(\kappa_1 + \kappa_2)$$

to ensure that stretching is additive and reversible. We choose

$$\xi = e^\kappa$$

to calculate the stretching factor. We satisfy the above requirement for any combination of reference and perturbed states since $e^{\kappa_1} * e^{\kappa_2} = e^{\kappa_1 + \kappa_2}$. In SeisMIC, we implement $\xi = e^\kappa$ to guarantee the linearity in the processing. To interpret measurements in the usual way as fractional velocity change, we use the approximation

$$\frac{dv}{v} = \frac{v' - \tilde{v}}{\tilde{v}} = \xi - 1 \approx \kappa$$

48 .

Utilising $\xi = 1 + \frac{dv}{v}$ for processing introduces nonlinearities and a dependency on the reference state. We note that this effect is not limited to measurements of the velocity change with the stretching method. Any manipulation

51 of $\frac{dv}{v}$ is affected and can be improved by working with $\kappa = \log(v'/\bar{v})$.

52 3 Additional Results of the Synthetic Spatial Imaging

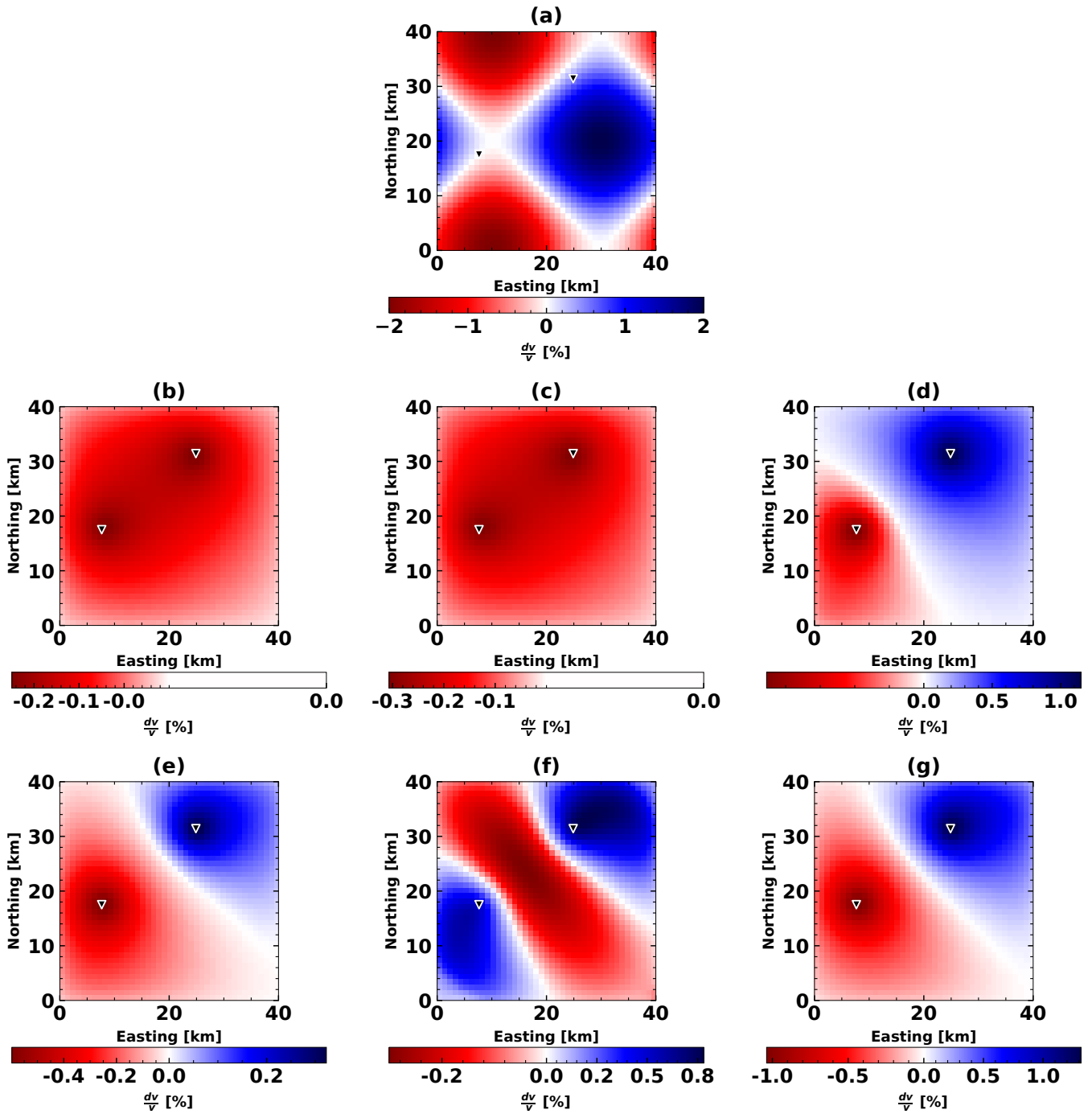


Figure 1 Examples of the spatial inversion using data from two stations, a model variance $\sigma_m = 0.5 \frac{\text{km}}{\text{km}^2}$, and a correlation length $\lambda = 2 \text{ km}$. **(a)** The synthetic velocity model and station configuration used. **(b)** Result of the spatial inversion using only cross-correlations and a single lapse time window. **(c)** Result of the spatial inversion using only cross-correlations and three lapse time windows. **(d)** Result of the spatial inversion using only auto-correlations and a single lapse time window. **(e)** Result of the spatial inversion using only auto-correlations and three lapse time windows. **(f)** Result of the spatial inversion from cross-correlations and auto correlations using a single lapse time window. **(g)** Result of the spatial inversion from cross-correlations and auto correlations using a single lapse time window.

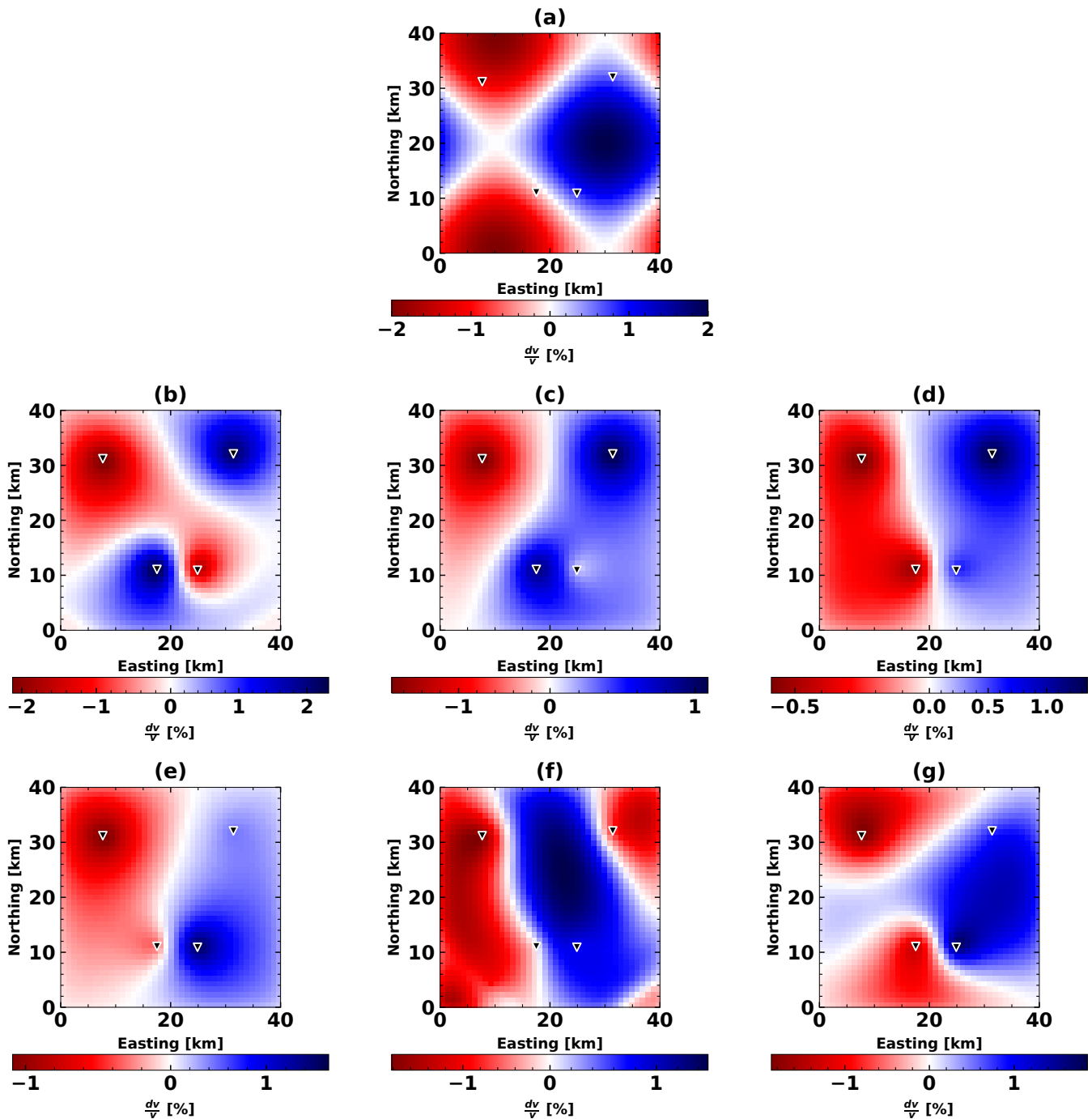


Figure 2 Examples of the spatial inversion using data from four stations, a model variance $\sigma_m = 0.25 \frac{\text{km}}{\text{km}^2}$, and a correlation length $\lambda = 2$ km. **(a)** The synthetic velocity model and station configuration used. **(b)** Result of the spatial inversion using only cross-correlations and a single lapse time window. **(c)** Result of the spatial inversion using only cross-correlations and three lapse time windows. **(d)** Result of the spatial inversion using only auto-correlations and a single lapse time window. **(e)** Result of the spatial inversion using only auto-correlations and three lapse time windows. **(f)** Result of the spatial inversion from cross-correlations and auto correlations using a single lapse time window. **(g)** Result of the spatial inversion from cross-correlations and auto correlations using a single lapse time window.

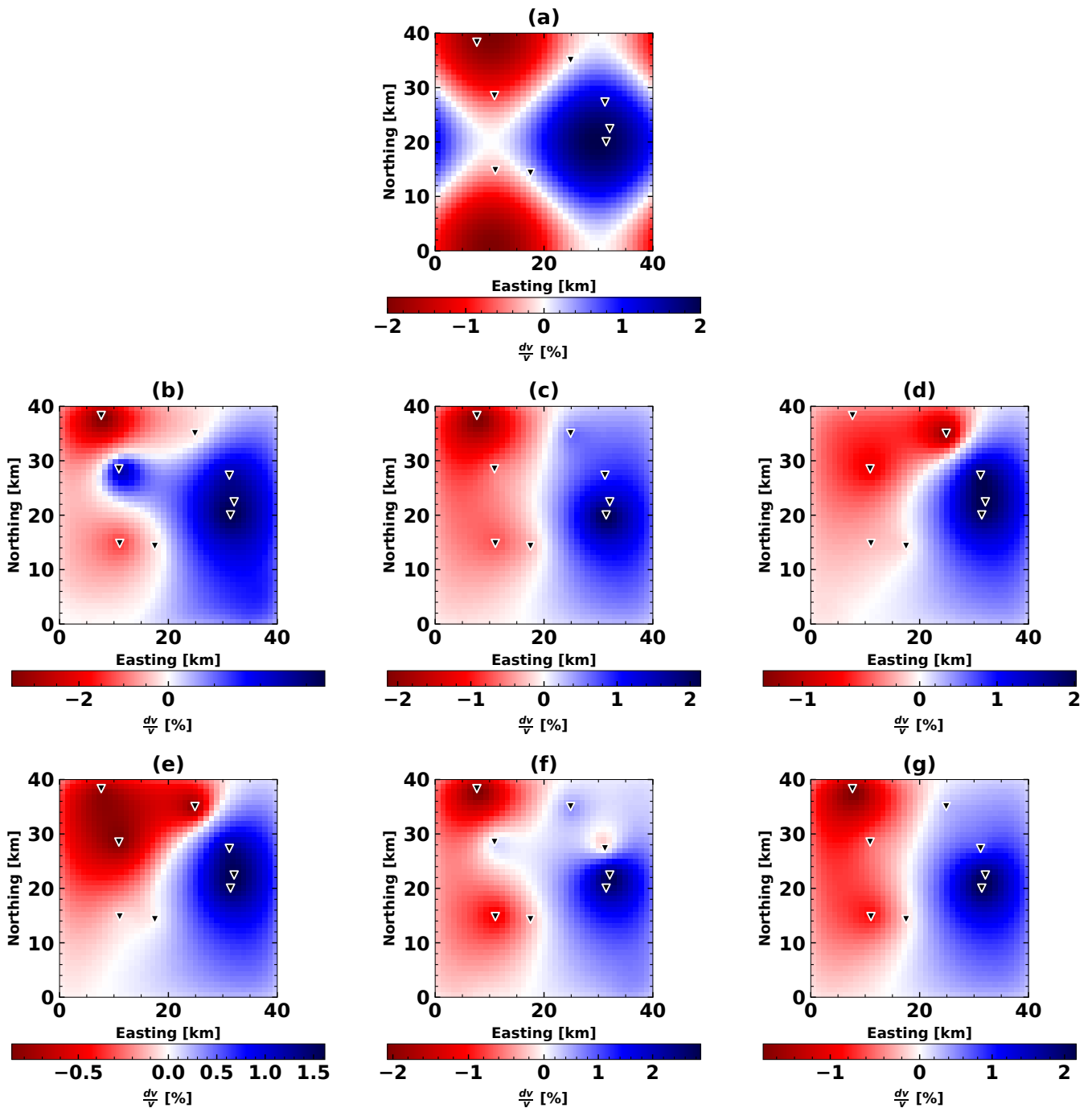


Figure 3 Examples of the spatial inversion using data from eight stations, a model variance $\sigma_m = 0.05 \frac{\text{km}}{\text{km}^2}$, and a correlation length $\lambda = 2$ km. **(a)** The synthetic velocity model and station configuration used. **(b)** Result of the spatial inversion using only cross-correlations and a single lapse time window. **(c)** Result of the spatial inversion using only cross-correlations and three lapse time windows. **(d)** Result of the spatial inversion using only auto-correlations and a single lapse time window. **(e)** Result of the spatial inversion using only auto-correlations and three lapse time windows. **(f)** Result of the spatial inversion from cross-correlations and auto correlations using a single lapse time window. **(g)** Result of the spatial inversion from cross-correlations and auto correlations using a single lapse time window.

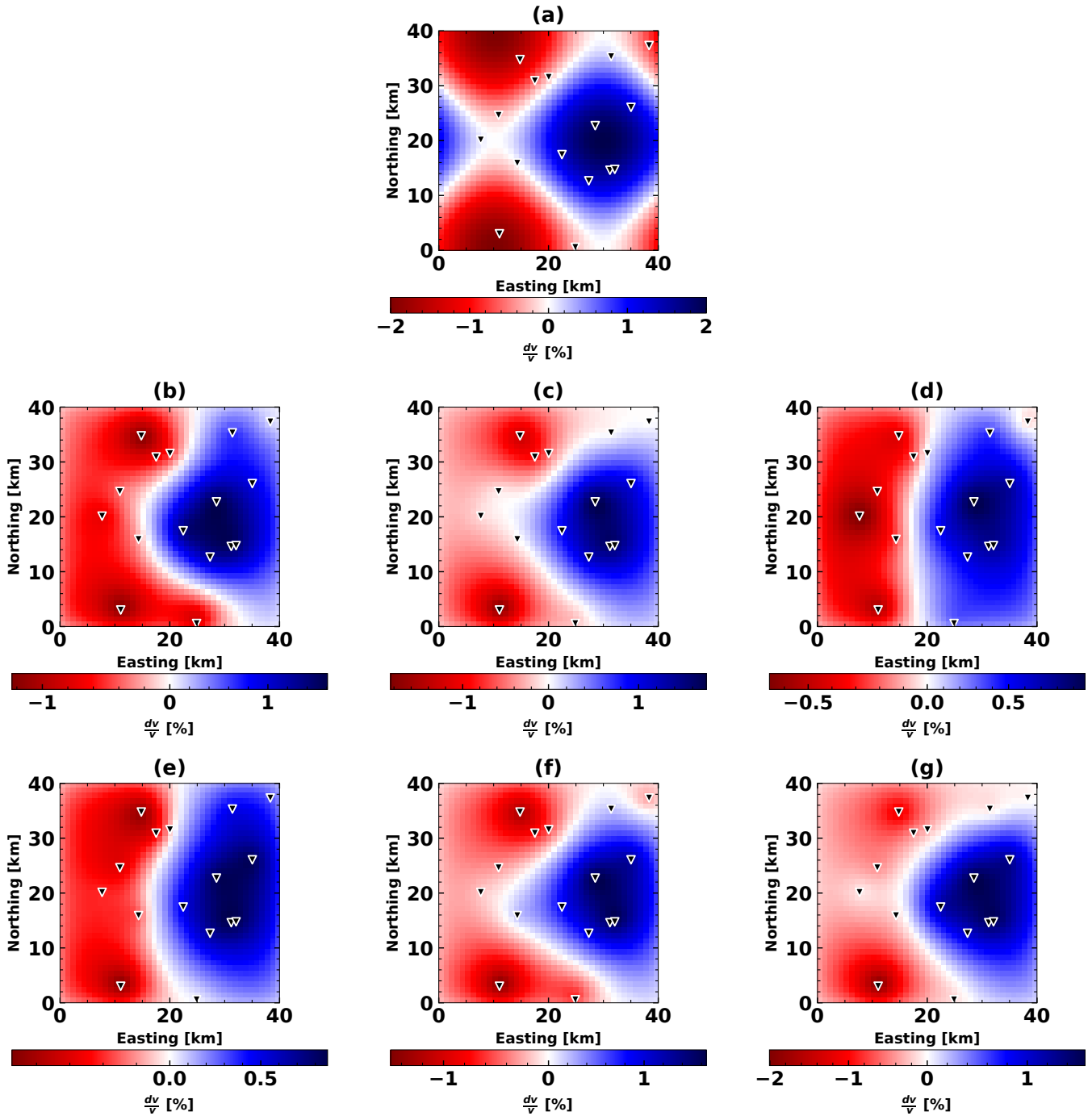


Figure 4 Examples of the spatial inversion using data from 16 stations, a model variance $\sigma_m = 0.02 \frac{\text{km}}{\text{km}^2}$, and a correlation length $\lambda = 2$ km. **(a)** The synthetic velocity model and station configuration used. **(b)** Result of the spatial inversion using only cross-correlations and a single lapse time window. **(c)** Result of the spatial inversion using only cross-correlations and three lapse time windows. **(d)** Result of the spatial inversion using only auto-correlations and a single lapse time window. **(e)** Result of the spatial inversion using only auto-correlations and three lapse time windows. **(f)** Result of the spatial inversion from cross-correlations and auto correlations using a single lapse time window. **(g)** Result of the spatial inversion from cross-correlations and auto correlations using a single lapse time window.

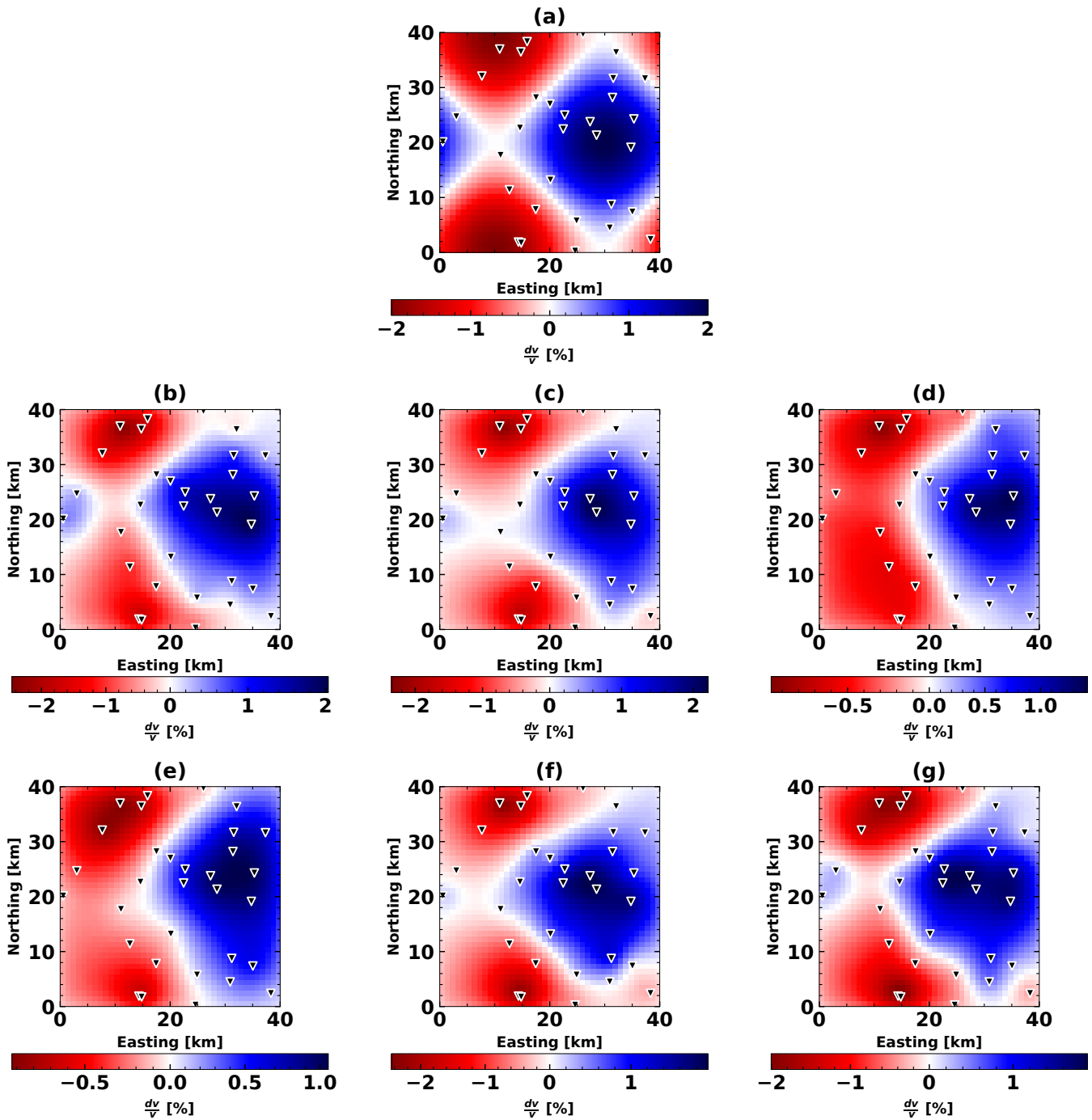


Figure 5 Examples of the spatial inversion using data from 32 stations a model variance $\sigma_m = 0.05 \frac{\text{km}}{\text{km}^2}$ and a correlation length $\lambda = 2 \text{ km}$. **(a)** The synthetic velocity model and station configuration used. **(b)** Result of the spatial inversion using only cross-correlations and a single lapse time window. **(c)** Result of the spatial inversion using only cross-correlations and three lapse time windows. **(d)** Result of the spatial inversion using only auto-correlations and a single lapse time window. **(e)** Result of the spatial inversion using only auto-correlations and three lapse time windows. **(f)** Result of the spatial inversion from cross-correlations and auto correlations using a single lapse time window. **(g)** Result of the spatial inversion from cross-correlations and auto correlations using a single lapse time window.